A Novel, Single-Layer Model for Composite Plates Using Local-Global Approach*

Shilei Han† and Olivier A. Bauchau‡
†University of Michigan-Shanghai Jiao Tong University Joint Institute
Shanghai, China 200240
‡Department of Aerospace Engineering, University of Maryland
College Park, Maryland 20742

Abstract

In structural analysis, many components are approximated as plates. More often that not, classical plate theories, such as Kirchhoff or Reissner-Mindlin plate theories, form the basis of the analytical developments. The advantage of these approaches is that they leads to simple kinematic descriptions of the problem: the plate's normal material line is assumed to remain straight and its displacement field is fully defined by three displacement and two rotation components. While such approach is capable of capturing the kinetic energy of the system accurately, it cannot represent the strain energy adequately. For instance, it is well known from three-dimensional elasticity theory that the normal material line will warp under load for laminated composite plates, leading to three-dimensional deformations that generate complex stress states. To overcome this problem, several layer-wise plate theories have been proposed. While these approaches work well for some cases, they often lead to inefficient formulations because they introduce numerous additional variables. This paper presents a novel, single-layer theory using local-global Approach: based on a finite element semi-discretization of the normal material line, the two-dimensional plate equations are derived from three-dimensional elasticity using a rigorous dimensional reduction procedure. Three-dimensional stresses through the plate's thickness can be recovered accurately from the plate's stress resultants.

1 Introduction

Plates are structural components for which one dimension is far smaller than the other two. The mid-plane of the plate lies along its two long dimensions, and the normal to the plate extends along the shorter dimension. The material properties of the plate are assumed to vary smoothly over the plate's mid-plane surface.

Numerous structures can be approximated as plates or shells. The long, slender wings of an aircraft can be analyzed, to a first approximation, as beams, but a more refined analysis will treat the upper and lower skins of the wing as thin plates or shells supported by ribs and longerons or stiffeners. The same can be said about helicopter or wind turbine blades. Buckling of the face sheets of wind turbine rotor blades is an important problem that cannot be captured by beam models. This instability, however, will be captured by plate models.

Solid mechanics theories describing plates, more commonly referred to as "plate theories," play an important role in structural analysis because they provide tools for the analysis of these commonly

European Journal of Mechanics - A/Solids, **60**: pp 1–16, 2016

used structural components. Although more sophisticated formulations, such as three-dimensional elasticity theory, could be used for the analysis of plates and shells, the associated computational burden is often too heavy. Plate theories reduce the analysis of complex, three-dimensional structures to two-dimensional problems. The main goal of the proposed plate theory is to approximate the three-dimensional plate-like structure with a two-dimensional model, while retaining an accurate representation of the local, three-dimensional stress and strain fields through the thickness of the plate.

Several plate theories have been developed based on various assumptions, and lead to different levels of accuracy. One of the simplest and most useful of these theories is due to Kirchhoff who analyzed the bending of thin plates. Kirchhoff plate theory [1, 2] is used commonly in many civil, mechanical and aerospace applications, although shear deformable plate theories [3, 4, 5], often called "Reissner-Mindlin plates," have also found wide acceptance.

In many applications, however, plates are complex built-up structures. In aeronautical constructions, for instance, the increased use of laminated composite materials leads to heterogeneous, highly anisotropic structures. Layers of anisotropic material are stacked through the thickness of the plate. This new type of structural component prompted the development of new plate theories [6, 7, 8], often based on classical lamination theory [9, 10].

Further refinements then followed with the goal of capturing the intricate three-dimensional stress field that develops under load, with special emphasis on interlaminar shear stresses. The various approaches fall into two categories: single-layer and layer-wise plate theories. Single-layer plate theories have been proposed by assuming higher-order or zigzag displacement fields for the entire normal material line [11, 12, 13, 14, 15]. In layer-wise theories [16, 17, 18], the displacement field of the normal material line for each layer is independent of that of the others, with a simple C_0 continuity conditions imposed at the layer boundaries. Although these approaches lead to higher accuracy, the number of unknowns increases considerably. More recently, Carrera [19, 20] proposed the "Carrera Unified Formulation" for the general description of two-dimensional formulations for multilayered plates and shells. This formulation is composed of a series of hierarchical models from simple, single-layer models up to higher-order layer-wise descriptions and provide a tool for the systematic assessment of different theories.

For plates, the aspect ratio is usually a small parameter and hence, the stress and displacement gradients over the plate's mid-surface are often smaller than those through its thickness. Based on this assumption, efficient single-layer plate models can be derived rigorously from three-dimensional elasticity through dimensional reduction techniques that split the original problem into a two-dimensional analysis over the plate's mid-plane surface and a one-dimensional, through-the-thickness linear analysis. The plate's stiffness matrix is a by-product of the dimensional reduction process, which also enables the recovery of three-dimensional stress fields. These approaches, derived from three-dimensional elasticity theory directly, can handle laminated plates and shells made of anisotropic composite materials without increasing the total number of unknowns.

Asymptotic and multiscale analysis methods have been the tools of choice for the derivation of single-layer models. Asymptotic and multiscale methods expand the solution in terms of the aspect ratio, leading to a rational decomposition of the three-dimensional problem into two-dimensional equations over the plate's mid-plane and a through-the-thickness problem. Based on this approach, Friedrichs and Dressler [21] and Kalamkarov [22] investigated isotropic and in-homogenous plate problems, respectively. A unified theory based on Variational Asymptotic Method [23, 24], (VAM), presenting both linear, one-dimensional through-the-thickness analysis, and nonlinear, two-dimensional analysis over the mid-plane surface of the plate or shell was developed by Sutyrin and Hodges [25, 26], and Yu *et al.* [27, 28]. More recently, Kim [29] proposed a finite element based asymptotic analysis for generally anisotropic plates.

It is not necessary to use asymptotic expansion methods to tackle plate analysis. A finite element based, semi-discretization approach was proposed Masarati and Ghiringhelli [30] to solve laminated

plate problems; they found solutions of the three-dimensional equilibrium equations through the thickness of the plate. These solutions then yield the plate's global compliance matrix and the local stress field can be recovered.

The Representative Volume Element (RVE) approach is a common tool for multiscale analysis. Gruttmann and Wagner [31] used a through-the-thickness RVE to develop local/global plate models. The displacement field of the RVE is split into rigid normal material line and warping components. The local RVE and global plate models are coupled at the lateral surfaces of the RVE and are solved simultaneously.

In this paper, a novel single-layer model for composite plates is developed by assuming the gradients of stress and displacement components over the plate's mid-surface to be smaller than those through its thickness. A semi-discretization of the general equations of three-dimensional elasticity is performed, defining the "local model." The equations relating the stress resultants, the plate's deformation measures, and the warping field of the normal material line are derived from a linear combination of the equations of the local model. These equations define the relationship between the stress resultants and deformation measures in an implicit manner, and hence, define the "global model." By means of a recursive process, power series solutions are found for the combined equations of the local and global models. Based on these solutions, the local problem for plate-like structures is reduced to the corresponding global problem, the single-layer model, and the local stress and strain fields can recovered from the global solution. The 8×8 stiffness matrix of the plate is a by-product of the reduction process; it takes into account warping effects due to material heterogeneity. Local stress and strain fields at any point through the thickness of the plate can be recovered from the global solution. The proposed method is applicable to anisotropic plates with arbitrarily complex through-the-thickness lay-up configurations.

2 Kinematics of the problem

Figure 1 depicts a flat plate of thickness h and a typical material line, denoted $\mathcal{L}$, normal to the midplane of the plate, $\mathcal{S}$. The volume of the plate, denoted as Ω, is generated by sliding the normal material line over the plate's midplane, *i.e.*, $\Omega = \mathcal{S} \times \mathcal{L}$. The plate's lateral boundary, $\partial\Omega$, is generated by sliding the normal material line over the midplane's boundary Γ, *i.e.*, $\partial\Omega = \Gamma \times \mathcal{L}$. Coordinates η_1 and η_2 define the plate's midplane, *i.e.*, they measure length along unit vectors $\bar{b}_1$ and $\bar{b}_2$, respectively. Point **B** is located at the intersection of the normal material line with the plate's midplane. The unit tangent vectors to midplane are defined as $\bar{b}_1 = \partial \underline{r}_B/\partial\eta_1$ and $\bar{b}_2 = \partial \underline{r}_B/\partial\eta_2$, where $\underline{r}_B(\eta_1, \eta_2)$ is the position vector of point **B** with respect to the origin of the inertial frame, $\mathcal{F} = [\mathbf{O}, \mathcal{I} = (\bar{\imath}_1, \bar{\imath}_2, \bar{\imath}_3)]$. The normal material line is aligned with unit vector $\bar{b}_3$, which is normal to both $\bar{b}_1$ and $\bar{b}_2$, and material frame $\mathcal{F}^* = \left[\mathbf{B}, \mathcal{B}^* = (\bar{b}_1, \bar{b}_2, \bar{b}_3)\right]$ is then defined. A set of material coordinates that naturally represents the configuration of the plate is selected as η_1, η_2, and η_3, where η_3 is the coordinate through the plate's thickness.

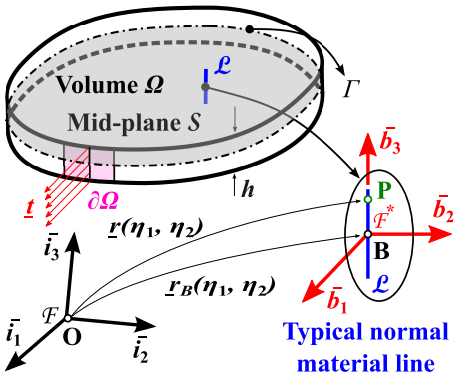

Figure 1: Configuration of the plate.

The rotation tensor that brings basis $\mathcal{I}$ to basis $\mathcal{B}^*$ is denoted $\underline{\underline{R}}$ and the following motion tensor [32] is defined

$$\underline{\underline{\mathcal{C}}} = \begin{bmatrix} \underline{\underline{R}} & \tilde{r}_B \underline{\underline{R}} \\ \underline{\underline{0}} & \underline{\underline{R}} \end{bmatrix}. \tag{1}$$

Motion tensor $\underline{\underline{\mathcal{C}}}$ represents a finite rigid-body motion from frame $\mathcal{F}$ to $\mathcal{F}^*$. The components of

the plate's generalized curvature tensors in its initial configuration, resolved in frame $\mathcal{F}^*$, are then defined as

$$\tilde{\mathcal{K}}_1^* = \underline{\underline{\mathcal{C}}}^{-1}\underline{\underline{\mathcal{C}}}_{,1}, \tag{2a}$$

$$\tilde{\mathcal{K}}_2^* = \underline{\underline{\mathcal{C}}}^{-1}\underline{\underline{\mathcal{C}}}_{,2}, \tag{2b}$$

where notation $(\cdot)^*$ indicates tensor components resolved in frame $\mathcal{F}^*$, and $(\cdot)_{,j} = \partial(\cdot)/\partial\eta_j$, $j = 1, 2, 3$, indicates a derivative with respect to span-wise variable η_j. Because the plate is flat, rotation tensor $\underline{\underline{R}}$ is independent of coordinates η_1 and η_2, and hence,

$$\tilde{\mathcal{K}}_1^* = \begin{bmatrix} \underline{\underline{0}} & \tilde{b}_1^* \\ \underline{\underline{0}} & \underline{\underline{0}} \end{bmatrix}, \tag{3a}$$

$$\tilde{\mathcal{K}}_2^* = \begin{bmatrix} \underline{\underline{0}} & \tilde{b}_2^* \\ \underline{\underline{0}} & \underline{\underline{0}} \end{bmatrix}, \tag{3b}$$

where notation $\tilde{b}$ indicates the skew symmetric matrix constructed from the components of vector $\underline{b}$, *i.e.*, $\underline{b} = \text{axial}(\tilde{b})$.

2.1 Position and base vectors in the reference configuration

With these definitions, the position vector of an arbitrary material point of the plate becomes

$$\underline{r}(\eta_1, \eta_2, \eta_3) = \underline{r}_B(\eta_1, \eta_2) + \eta_3\bar{b}_3 = \underline{r}_B(\eta_1, \eta_2) + \underline{q}(\eta_3), \tag{4}$$

where vector $\underline{q} = \underline{r} - \underline{r}_B = \eta_3\bar{b}_3$ defines the relative position of material point $\mathbf{P}$ with respect to point $\mathbf{B}$.

The base vectors associated with these material coordinates are $\underline{g}_1 = \underline{r}_{,1} = \bar{b}_1$, $\underline{g}_2 = \underline{r}_{,1} = \bar{b}_2$, and $\underline{g}_3 = \underline{r}_{,3} = \bar{b}_3$. The components of these base vectors resolved in basis $\mathcal{B}^*$ are found as $\underline{g}_1^{*T} = \{1, 0, 0\}$, $\underline{g}_2^{*T} = \{0, 1, 0\}$, and $\underline{g}_3^{*T} = \{0, 0, 1\}$.

2.2 Position and base vectors in the deformed configuration

It is assumed that the plate undergoes small motions and that strains remain very small at all times. The plate's displacement field is now decomposed as a rigid normal-material-line motion and an additional warping field. Because expression "rigid normal-material-line motion" is wordy, it will be abbreviated as "rigid-normal motion" in the sequel. The rigid-normal motion generates strains because it is not a rigid-body motion of the entire plate. The rigid-normal motion is characterized by five degrees of freedom only, three displacements and two rotations, because the rotation of the normal line about its own axis, called "drilling rotation," is immaterial.

The infinitesimal rigid-normal motion is denoted as $\underline{\mathcal{U}}^*(\eta_1, \eta_2) = \{u_{R1}^*,\ u_{R2}^*,\ u_{R3}^*,\ -\phi_{R2}^*,\ \phi_{R1}^*,\ 0\}$, where $(\cdot)^*$ indicates components resolved in basis $\mathcal{B}^*$, u_{Ri}^*, $i = 1, 2, 3$, are the displacement components of point $\mathbf{B}$, and to be consistent with the conventional notations, the rotation about axis $\bar{b}_1$ and $\bar{b}_2$ are denoted as $-\phi_{R2}^*$ and ϕ_{R1}^*, respectively. The infinitesimal displacement field of the plate due to the rigid-normal motion, $\underline{\mathcal{U}}^*$, can be expressed as

$$\begin{Bmatrix} u_1^* \\ u_2^* \\ u_3^* \end{Bmatrix} = \begin{bmatrix} 1 & 0 & 0 & 0 & \eta_3 & 0 \\ 0 & 1 & 0 & -\eta_3 & 0 & 0 \\ 0 & 0 & 1 & 0 & 0 & 0 \end{bmatrix} \underline{\mathcal{U}}^* = \underline{\underline{z}}\,\underline{\mathcal{U}}^*. \tag{5}$$

The warping field is denoted $\underline{w}^*(\eta_1, \eta_2, \eta_3)$ and describes the displacement of a material point with respect to its position subsequent to the rigid-normal motion, see fig. 1. The proposed decomposition

is redundant because the arbitrary warping field also contains a rigid-normal motion. This ambiguity of the formulation will be resolved later, based on physical arguments presented in section 3. After deformation, the position vector of a material point becomes

$$\underline{R}(\eta_1,\eta_2,\eta_3) = \underline{r} + \underline{\underline{R}}\left(\underline{\underline{z}}\,\underline{\mathcal{U}}^*_R + \underline{w}^*\right). \tag{6}$$

The components of the base vectors in the deformed configuration, resolved in basis $\mathcal{B}^*$ are

$$\underline{G}^*_1 = \underline{g}^*_1 + \underline{\underline{z}}\,\underline{\mathcal{U}}^*_{,1} + \underline{w}^*_{,1}, \tag{7a}$$
$$\underline{G}^*_2 = \underline{g}^*_2 + \underline{\underline{z}}\,\underline{\mathcal{U}}^*_{,2} + \underline{w}^*_{,2}, \tag{7b}$$
$$\underline{G}^*_3 = \underline{g}^*_3 + \underline{\underline{z}}_{,3}\,\underline{\mathcal{U}}^* + \underline{w}^*_{,3}. \tag{7c}$$

2.3 Strain components

With these expressions, the components of the deformation gradient tensor resolved in basis $\mathcal{B}^*$ are $\underline{\underline{F}}^* = [\underline{G}^*_1\ \underline{G}^*_2\ \underline{G}^*_3]\ [\underline{g}^*_1\ \underline{g}^*_2\ \underline{g}^*_3]^{-1}$ and the corresponding infinitesimal strain tensor is $\underline{\underline{\gamma}}^* = (\underline{\underline{F}}^* + \underline{\underline{F}}^{*T})/2 - \underline{\underline{I}}$. For simplicity, the components of the strain tensor are collected into a single array as $\underline{\gamma}^{*T} = \{\gamma^*_{11},\ \gamma^*_{22},\ \gamma^*_{33},\ 2\gamma^*_{23},\ 2\gamma^*_{13},\ 2\gamma^*_{12}\}$. Explicit expressions of the strain components are then obtained from

$$\underline{\gamma}^* = \underline{\underline{g}}\,\underline{\mathcal{E}}^* + \underline{v}^* + \underline{\underline{B}}\,\underline{w}^*, \tag{8}$$

where matrix $\underline{\underline{g}}$ and operator matrix $\underline{\underline{B}}$ are defined in A. Array $\underline{\mathcal{E}}^*$, which stores the plate's eight sectional strain components, is defined as $\underline{\mathcal{E}}^{*T} = \{u^*_{R1,1}, u^*_{R2,2}, u^*_{R1,2} + u^*_{R2,1}, u^*_{3R,1} + \theta^*_{R1}, u^*_{3R,2} + \theta^*_{R2}, \theta^*_{R1,1}, \theta^*_{R2,2}, \theta^*_{R2,1} + \theta^*_{R1,2}\}$. A compact form of the array is found as

$$\underline{\mathcal{E}}^* = \underline{\underline{\mathfrak{t}}}_1\left(\underline{\mathcal{U}}^*_{,1} + \tilde{\mathcal{K}}^*_1\underline{\mathcal{U}}^*\right) + \underline{\underline{\mathfrak{t}}}_2\left(\underline{\mathcal{U}}^*_{,2} + \tilde{\mathcal{K}}^*_2\underline{\mathcal{U}}^*\right), \tag{9}$$

where Boolean matrices $\underline{\underline{\mathfrak{t}}}_1$ and $\underline{\underline{\mathfrak{t}}}_2$ are defined in eq. (53). In eq. (8), the array of warping derivatives, $\underline{v}^*$, is defined as

$$\underline{v}^* = \underline{\underline{\mathfrak{b}}}^T_1\underline{w}^*_{,1} + \underline{\underline{\mathfrak{b}}}^T_2\underline{w}^*_{,2}, \tag{10}$$

and matrices $\underline{\underline{\mathfrak{b}}}_1$ and $\underline{\underline{\mathfrak{b}}}_2$ are given by eq. (52). Clearly, the first term of eq. (8) represents the strains due to rigid-normal motion, and the last two terms stem from the effects of local warping.

Taking variation of the sectional strain measures, leads to

$$\delta\underline{\mathcal{E}}^* = \underline{\underline{\mathfrak{t}}}_1(\underline{\delta\mathcal{U}}^*_{,1} + \tilde{\mathcal{K}}^*_1\underline{\delta\mathcal{U}}^*) + \underline{\underline{\mathfrak{t}}}_2(\underline{\delta\mathcal{U}}^*_{,2} + \tilde{\mathcal{K}}^*_2\underline{\delta\mathcal{U}}^*). \tag{11}$$

2.4 Semi-discretization

Plate theory is characterized by two-dimensional differential equations governing the displacement field assumed to be a function of the in-plane variables, η_1 and η_2, only. In the above paragraphs, the displacement field has been treated as a general vector field depending on three independent variables, η_1, η_2, and η_3. To obtain a two-dimensional formulation, the following semi-discretizations of the warping field $\underline{w}^*$ and of its partial derivative $\underline{v}^*$ are performed,

$$\underline{w}^*(\eta_1,\eta_2,\eta_3) = \underline{\underline{N}}(\eta_3)\underline{\hat{w}}(\eta_1,\eta_2), \tag{12a}$$
$$\underline{v}^*(\eta_1,\eta_2,\eta_3) = \underline{\underline{H}}(\eta_3)\underline{\hat{v}}(\eta_1,\eta_2), \tag{12b}$$

where matrices $\underline{\underline{N}}(\eta_3)$ and $\underline{\underline{H}}(\eta_3)$ store the one-dimensional shape functions used in the discretization. Arrays $\underline{\hat{w}}(\eta_1,\eta_2)$ and $\underline{\hat{v}}(\eta_1,\eta_2)$ store the nodal values of the warping field and its derivatives. Let N be the number of nodes used to discretize the plate's normal material line; then $\underline{\hat{w}}$ and $\underline{\hat{v}}$ are of size $3N$ and $6N$, respectively.

Equations (12) correspond to a *semi-discretization* of the problem. Figure 2 depicts the finite element mesh that extends over the plate's normal material line only and the nodal values of the displacement components remain functions of the in-plane variables, η_1 and η_2 (For clarity, stress vectors are shown on two faces of the differential element only). The semi-discretization procedure leads to a numerical treatment of the solution for variable η_3 whereas the dependency of the solution on variables η_1 and η_2 is treated analytically. Introducing this discretization into eq. (8) yields the components of tensor as

$$\underline{\gamma}^* = \underline{\underline{g}}\,\underline{\mathcal{E}}^* + \underline{\underline{H}}\,\underline{\hat{v}} + \underline{\underline{B}}\,\underline{\underline{N}}\,\underline{\hat{w}}. \tag{13}$$

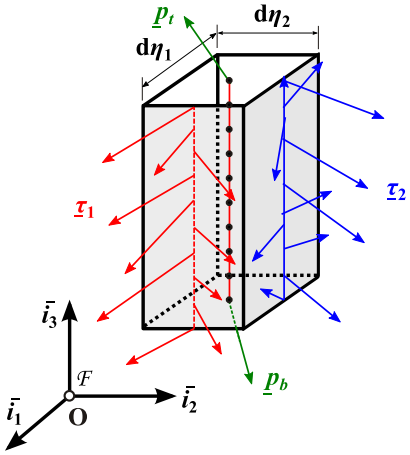

Figure 2: Semi-discretization of the plate.

3 Governing equations

The plate's governing equations will be derived from the principle of virtual work, which states that $\delta A - \delta W = 0$, where δA and δW denote the variation of strain energy and virtual work done by the external forces, respectively. These quantities will be evaluated in sections 3.1 and 3.3, respectively.

3.1 The strain energy density

It is assumed that the plate is made of linear anisotropic material laminated through the thickness. Let $\underline{\underline{\mathcal{D}}}^*$ denote the 6×6 material stiffness matrix resolved the material basis. Using the discretized components of strain tensor given by eq. (13), the strain energy per unit area of the plate, defined as $\mathfrak{a} = 1/2 \int_{\mathcal{L}} \delta\underline{\gamma}^{*T} \underline{\underline{\mathcal{D}}}^* \underline{\gamma}^* \, \mathrm{d}\eta_3$, becomes

$$\mathfrak{a} = \frac{1}{2}(\underline{\hat{v}} + \underline{\underline{G}}\,\underline{\mathcal{E}}^*)^T \left[\underline{\underline{M}}(\underline{\hat{v}} + \underline{\underline{G}}\,\underline{\mathcal{E}}^*) + \underline{\underline{C}}^T \underline{\hat{w}}\right] + \frac{1}{2}\underline{\hat{w}}^T \left[\underline{\underline{C}}(\underline{\hat{v}} + \underline{\underline{G}}\,\underline{\mathcal{E}}^*) + \underline{\underline{E}}\,\underline{\hat{w}}\right], \tag{14}$$

where matrix $\underline{\underline{G}}$ stacks the rows of matrix $\underline{\underline{g}}$ for each of the nodes, and matrices $\underline{\underline{M}}$, $\underline{\underline{C}}$, and $\underline{\underline{E}}$ are defined as

$$\underline{\underline{M}} = \int_{\mathcal{L}} \underline{\underline{H}}^T \underline{\underline{\mathcal{D}}}^* \underline{\underline{H}} \, \mathrm{d}\mathcal{L}, \tag{15a}$$

$$\underline{\underline{C}} = \int_{\mathcal{L}} (\underline{\underline{B}}\,\underline{\underline{N}})^T \underline{\underline{\mathcal{D}}}^* \underline{\underline{H}} \, \mathrm{d}\mathcal{L}, \tag{15b}$$

$$\underline{\underline{E}} = \int_{\mathcal{L}} (\underline{\underline{B}}\,\underline{\underline{N}})^T \underline{\underline{\mathcal{D}}}^* (\underline{\underline{B}}\,\underline{\underline{N}}) \, \mathrm{d}\mathcal{L}. \tag{15c}$$

Given the distribution of material stiffness properties, these matrices can be evaluated by integration through the thickness of the plate. With these definitions, the plate's strain energy can be found as $A = \int_{\mathcal{S}} \mathfrak{a} \, \mathrm{d}\eta_1 \mathrm{d}\eta_2$.

3.2 Nodal forces and stress resultants

As was done for the components of the strain tensor in eq. (8), the components of stress tensor are stored in a single array, denoted $\underline{\tau}^* = \{\underline{\tau}^*_{11}\ \underline{\tau}^*_{22}\ \underline{\tau}^*_{33}\ \underline{\tau}^*_{23}\ \underline{\tau}^*_{13}\ \underline{\tau}^*_{12}\}^T$. Figure 2 shows a differential element of the plate subjected to stresses applied over its four vertical faces. Stress vectors $\underline{\tau}^*_1 = \underline{\underline{\mathfrak{b}}}_1 \underline{\tau}^*$

and $\underline{\tau}_2^* = \underline{\underline{\mathfrak{b}}}_2 \underline{\tau}^*$ are acting on the faces normal to unit vectors $\bar{b}_1$ and $\bar{b}_2$, respectively. Accordingly, the arrays of nodal forces acting on faces normal to unit vectors $\bar{\imath}_1$ and $\bar{\imath}_2$ can be found as $\underline{\hat{P}}_1 = \int_{\mathcal{L}} \underline{\underline{N}}^T \underline{\tau}_1^* \, \mathrm{d}\eta_3$ and $\underline{\hat{P}}_2 = \int_{\mathcal{L}} \underline{\underline{N}}^T \underline{\tau}_1^* \, \mathrm{d}\eta_3$. Introducing the discretized components of strain tensor given by eq. (13) and material constitutive laws $\underline{\tau}^* = \underline{\underline{\mathcal{D}}}^* \underline{\gamma}^*$ into the nodal forces yields

$$\underline{\hat{P}}_1 = \frac{\partial \mathfrak{a}}{\partial \underline{\hat{w}}_{,1}} = \underline{\underline{\hat{\mathfrak{b}}}}_1 \underline{\hat{P}}, \tag{16a}$$

$$\underline{\hat{P}}_2 = \frac{\partial \mathfrak{a}}{\partial \underline{\hat{w}}_{,2}} = \underline{\underline{\hat{\mathfrak{b}}}}_2 \underline{\hat{P}}, \tag{16b}$$

where matrices $\underline{\underline{\hat{\mathfrak{b}}}}_1 = \mathrm{diag}(\underline{\underline{\mathfrak{b}}}_1)$ and $\underline{\underline{\hat{\mathfrak{b}}}}_2 = \mathrm{diag}(\underline{\underline{\mathfrak{b}}}_2)$ gather the corresponding counterparts at each node, and array $\underline{\hat{P}}$ is defined as

$$\underline{\hat{P}} = \frac{\partial \mathfrak{a}}{\partial \underline{\hat{v}}} = \underline{\underline{M}} \, \underline{\hat{v}} + \underline{\underline{C}} \, \underline{\hat{w}}. \tag{17}$$

The summation of forces acting along the normal material line on the face normal to unit vector $\bar{b}_1$ is $\underline{f}_1^* = \int_{\mathcal{L}} \underline{\tau}_1^* \, \mathrm{d}\eta_3$, and the sum of the moments is $\underline{m}_1^* = \int_{\mathcal{L}} \underline{q}^{*T} \underline{\tau}_1^* \, \mathrm{d}\eta_3$. Similar observations hold for the stress resultants acting on a face normal to unit vector $\bar{b}_2$. Introducing the discretized components of strain tensor given by eq. (13), the nodal forces defined by eq. (16), and matrix $\underline{\underline{z}}$ defined by eq. (5), the stress resultants become

$$\underline{\mathcal{F}}_1^* = \begin{Bmatrix} \underline{f}_1^* \\ \underline{m}_1^* \end{Bmatrix} = \underline{\underline{Z}}^T \underline{\hat{P}}_1, \quad \underline{\mathcal{F}}_2^* = \begin{Bmatrix} \underline{f}_2^* \\ \underline{m}_2^* \end{Bmatrix} = \underline{\underline{Z}}^T \underline{\hat{P}}_2, \tag{18}$$

where $\underline{\mathcal{F}}_1^*$ and $\underline{\mathcal{F}}_2^*$ are the array of stress resultants on faces normal to unit vectors $\bar{b}_1$ and $\bar{b}_2$, respectively, resolved in the material basis, and matrix $\underline{\underline{Z}}$ stack the rows of matrix $\underline{\underline{z}}$ for each of the nodes.

Stress resultants $\underline{\mathcal{F}}_1^*$ and $\underline{\mathcal{F}}_2^*$ are not independent but consist both of a subset of the eight independent stress resultant stored in the array $\underline{\mathcal{F}}^{*T} = \{N_1^*, N_2^*, N_{12}^*, Q_1^*, Q_2^*, M_1^*, M_2^*, M_{12}^*\}$, where N_1^*, N_2^*, and N_{12}^* are the in-plane forces, Q_1^* and Q_2^* the transverse shear forces, and M_1^*, M_2^*, and M_{12}^* the bending moments. It then follows that

$$\underline{\mathcal{F}}_1^* = \underline{\underline{\mathfrak{t}}}_1 \underline{\mathcal{F}}^*, \tag{19a}$$

$$\underline{\mathcal{F}}_2^* = \underline{\underline{\mathfrak{t}}}_2 \underline{\mathcal{F}}^*, \tag{19b}$$

where matrices $\underline{\underline{\mathfrak{t}}}_1$ and $\underline{\underline{\mathfrak{t}}}_2$ are defined in eqs. (53). The following matrix identities are verified easily

$$\underline{\underline{\hat{\mathfrak{b}}}}_1^T \underline{\underline{Z}} = \underline{\underline{G}} \, \underline{\underline{\mathfrak{t}}}_1^T, \tag{20a}$$

$$\underline{\underline{\hat{\mathfrak{b}}}}_2^T \underline{\underline{Z}} = \underline{\underline{G}} \, \underline{\underline{\mathfrak{t}}}_2^T. \tag{20b}$$

Finally, the explicit expression of $\underline{\mathcal{F}}^*$ is found as

$$\underline{\mathcal{F}}^* = \underline{\underline{G}}^T \underline{\hat{P}} = (\underline{\underline{G}}^T \underline{\underline{M}} \, \underline{\underline{G}}) \underline{\mathcal{E}}^* + (\underline{\underline{M}} \, \underline{\underline{G}})^T \underline{\hat{v}} + (\underline{\underline{C}} \, \underline{\underline{G}})^T \underline{\hat{w}}. \tag{21}$$

Note that this expression defines the global strain components in terms of the rigid-normal motion, $\underline{\mathcal{U}}^*$, which is as yet undefined. In the absence of warping, *i.e.*, when $\underline{\hat{w}} = \underline{0}$, eq. (21) reduces to $\underline{\mathcal{F}}^* = \underline{\underline{\mathcal{C}}}_{RM}^* \underline{\mathcal{E}}^*$, where $\underline{\underline{\mathcal{C}}}_{RM}^* = \underline{\underline{G}}^T \underline{\underline{M}} \, \underline{\underline{G}}$ is the Reissner-Mindlin stiffness matrix. Indeed, Reissner-Mindlin plate theory [3, 5] postulates that normal material lines remain straight, implying that the sectional displacement field is captured adequately by the rigid-normal motion described by matrix $\underline{\underline{Z}}$. The last two terms of eq. (21) describe the change in the sectional stiffness resulting from warping deformation.

In eq. (21), if the warping displacements, $\underline{\hat{w}}$, and their derivatives, $\underline{\hat{w}}_{,1}$ and $\underline{\hat{w}}_{,2}$, can be expressed in terms of the stress resultants, an equivalent global stiffness matrix can be found. Clearly, the determination of the warping field is key to the accurate evaluation of the plate's global stiffness matrix.

3.3 The virtual work done by the externally applied loads

As shown in fig. 2, the plate is subjected to three types of loading: surface tractions, $\underline{p}_t$ and $\underline{p}_b$, applied at the plate's top and bottom surfaces, respectively, and body forces, $\underline{b}$. In addition, the plate subjected to surface tractions, $\underline{t}^*$, over its lateral boundary $\partial\Omega$, see fig. 1. The corresponding displacements, expressed as combinations of a rigid-normal motion and warping, are denoted $\underline{u}_t^* = \underline{\underline{z}}_t\underline{\mathcal{U}}^* + \underline{w}_t^*$, $\underline{u}_b^* = \underline{\underline{z}}_b\underline{\mathcal{U}}^* + \underline{w}_b^*$, $\hat{\underline{u}}^* = \underline{\underline{z}}\underline{\mathcal{U}}^* + \underline{w}^*$, and $\hat{\underline{u}}_\ell^* = \underline{\underline{z}}_\ell\underline{\mathcal{U}}^* + \underline{w}^*$, respectively. The virtual work done by these externally applied loads is then

$$\begin{aligned}\delta W &= \int_{\mathcal{S}}\left(\delta\underline{u}_t^{*T}\underline{p}_t^* + \delta\underline{u}_b^{*T}\underline{p}_b^* + \int_{\mathcal{L}}\delta\underline{u}^{*T}\underline{b}^*\ \mathrm{d}\eta_3\right)\mathrm{d}\eta_1\mathrm{d}\eta_2 + \int_{\partial\Omega}\underline{u}_\ell^{*T}\underline{t}^*\mathrm{d}\eta_3\mathrm{d}s \\ &= \int_{\mathcal{S}}\left(\delta\underline{\mathcal{U}}^{*T}\underline{\mathcal{A}} + \delta\underline{\hat{w}}^T\underline{Q}\right)\ \mathrm{d}\eta_1\mathrm{d}\eta_2 + \int_\Gamma\left(\delta\underline{\mathcal{U}}^{*T}\underline{\bar{\mathcal{F}}}^* + \delta\underline{\hat{w}}^T\underline{\bar{P}}\right)\ \mathrm{d}s,\end{aligned} \tag{22}$$

where s denote the arc-length coordinate along contour Γ. Loading vectors $\underline{Q}$ and $\underline{\bar{P}}$ are found by introducing the discretized displacement field given by eq. (12) in the second equality to find $\underline{Q} = \underline{\underline{N}}^T(h/2)\underline{p}_t^* + \underline{\underline{N}}^T(-h/2)\underline{p}_b^* + \int_{\mathcal{L}}\underline{\underline{N}}^T\underline{b}^*\ \mathrm{d}\eta_3$ and $\underline{\bar{P}} = \int_{\mathcal{L}}\underline{\underline{N}}^T\underline{t}^*\ \mathrm{d}\eta_3$. Similarly, $\underline{\mathcal{A}} = \underline{\underline{Z}}^T\underline{Q}$ and $\underline{\bar{\mathcal{F}}}^* = \underline{\underline{Z}}^T\underline{\bar{P}}$ are the resultant of the externally applied loads.

3.4 Governing equations

Both global and local equilibrium equations will be obtained from the principle of virtual work, $\delta A - \delta W = 0$. Introducing the strain energy density (14) and virtual work done by the external loads (22) and integrating by parts leads to

$$\begin{aligned}&\int_{\mathcal{S}}\delta\underline{\hat{w}}^T\left[-\underline{\hat{P}}_{1,1} - \underline{\hat{P}}_{2,2} + \underline{\underline{C}}(\underline{\hat{v}} + \underline{\underline{G}}\,\underline{\mathcal{E}}^*) + \underline{\underline{E}}\,\underline{\hat{w}} - \underline{Q}\right] \\ &-\underline{\delta\mathcal{U}}^T\left(\underline{\mathcal{F}}_{1,1}^* - \underline{\tilde{\mathcal{K}}}_1^{*T}\underline{\mathcal{F}}_1^* + \underline{\mathcal{F}}_{2,2}^* - \underline{\tilde{\mathcal{K}}}_2^{*T}\underline{\mathcal{F}}_2^* + \underline{\mathcal{A}}\right)\ \mathrm{d}\eta_1\mathrm{d}\eta_2 \\ &+\int_\Gamma\ \delta\underline{\hat{w}}^T\left(\underline{\hat{P}}_n - \underline{\bar{P}}\right) + \underline{\mathcal{U}}^{*T}\left(\underline{\mathcal{F}}_n^* - \underline{\bar{F}}^*\right)\ \mathrm{d}s = 0,\end{aligned} \tag{23}$$

where the variation of the sectional strains was defined by eq. (11). Array $\underline{\hat{P}}_n$ and $\underline{\mathcal{F}}_n^*$ represent the nodal forces and resultants on the boundary and can be expressed as combinations of $\underline{\hat{P}}_j$ and $\underline{\mathcal{F}}_j^*$, $j = 1, 2$, respectively.

In the statement of the principle of virtual work, eq. (23), variations of the warping field, $\delta\underline{\hat{w}}$, and of the rigid-normal motion, $\underline{\delta\mathcal{U}}^*$, are not independent because the warping field includes a rigid-body motion. These variations, however, will be treated as independent and yield two sets of equilibrium equations: the global equations describing plate's overall motion and the local equations imposing through-the-thickness equilibrium. These two sets are correct but not independent; integration of the local equilibrium equations through the shell's thickness yields the global equilibrium equations.

First, the vanishing of the coefficients of virtual rigid-normal motion, $\underline{\delta\mathcal{U}}^*$, over the plate's mid-plane surface, $\mathcal{S}$, yields the plate's global equilibrium equations,

$$\underline{\mathcal{F}}_{1,1}^* - \underline{\tilde{\mathcal{K}}}_1^{*T}\underline{\mathcal{F}}_1^* + \underline{\mathcal{F}}_{2,2}^* - \underline{\tilde{\mathcal{K}}}_2^{*T}\underline{\mathcal{F}}_2^* = -\underline{\mathcal{A}}. \tag{24}$$

Next, the vanishing of the coefficients of virtual warping field, $\delta\underline{\hat{w}}$, over the plate's volume, Ω, yields the local equilibrium equations of the problem

$$\underline{\hat{P}}_{1,1} + \underline{\hat{P}}_{2,2} - \underline{\underline{C}}(\underline{\hat{v}} + \underline{\underline{G}}\,\underline{\mathcal{E}}^*) - \underline{\underline{E}}\,\underline{\hat{w}} = -\underline{Q}. \tag{25}$$

Introducing the nodal forces from eq. (16) and combining the results with eq. (21) yields

$$\underline{\breve{\underline{\underline{M}}}}_{11}\underline{\mathcal{X}}_{,11} + \underline{\breve{\underline{\underline{M}}}}_{12}\underline{\mathcal{X}}_{,12} + \underline{\breve{\underline{\underline{M}}}}_{22}\underline{\mathcal{X}}_{,22} + \underline{\breve{\underline{\underline{H}}}}_1\underline{\mathcal{X}}_{,1} + \underline{\breve{\underline{\underline{H}}}}_2\underline{\mathcal{X}}_{,2} - \underline{\breve{\underline{\underline{E}}}}\,\underline{\mathcal{X}} = -\underline{\mathcal{Q}}, \tag{26}$$

where the following arrays were defined

$$\underline{\mathcal{X}} = \begin{Bmatrix} \underline{\hat{w}} \\ \underline{\mathcal{E}}^* \end{Bmatrix}, \quad \underline{\mathcal{Q}} = \begin{Bmatrix} \underline{Q} \\ \underline{\mathcal{F}}^* \end{Bmatrix} \tag{27}$$

Linear system (26) is a hybrid system that combines the local and global equilibrium equations. The local problem consists of the equilibrium equations of three-dimensional elasticity written in terms of nodal displacements whereas the global problem consists of the plate equations written in terms of stress resultants and global strain measures. These combined equations link the local and global problems in a formal manner.

Linear system (26) features $N_T = 3N + 8$ unknowns, the $3N$ nodal displacements and the 8 global strain measures. The following matrices, each of size $N_T \times N_T$, have been defined

$$\breve{\underline{\underline{M}}}_{11} = \begin{bmatrix} \underline{\underline{M}}_{11} & \underline{\underline{0}} \\ \underline{\underline{0}} & \underline{\underline{0}} \end{bmatrix}, \; \breve{\underline{\underline{M}}}_{12} = \begin{bmatrix} \underline{\underline{M}}_{12} + \underline{\underline{M}}_{12}^T & \underline{\underline{0}} \\ \underline{\underline{0}} & \underline{\underline{0}} \end{bmatrix}, \; \breve{\underline{\underline{M}}}_{22} = \begin{bmatrix} \underline{\underline{M}}_{22} & \underline{\underline{0}} \\ \underline{\underline{0}} & \underline{\underline{0}} \end{bmatrix}, \tag{28a}$$

$$\breve{\underline{\underline{H}}}_1 = \begin{bmatrix} \underline{\underline{C}}_1^T - \underline{\underline{C}}_1 & (\hat{\underline{\mathfrak{b}}}_1 \underline{\underline{M}}\, \underline{\underline{G}}) \\ -(\hat{\underline{\mathfrak{b}}}_1 \underline{\underline{M}}\, \underline{\underline{G}})^T & \underline{\underline{0}} \end{bmatrix}, \; \breve{\underline{\underline{H}}}_2 = \begin{bmatrix} \underline{\underline{C}}_2^T - \underline{\underline{C}}_2 & (\hat{\underline{\mathfrak{b}}}_2 \underline{\underline{M}}\, \underline{\underline{G}}) \\ -(\hat{\underline{\mathfrak{b}}}_2 \underline{\underline{M}}\, \underline{\underline{G}})^T & \underline{\underline{0}} \end{bmatrix}, \tag{28b}$$

$$\breve{\underline{\underline{E}}} = \begin{bmatrix} \underline{\underline{E}} & (\underline{\underline{C}}\, \underline{\underline{G}}) \\ (\underline{\underline{C}}\, \underline{\underline{G}})^T & \underline{\underline{\mathcal{C}}}^*_{RM} \end{bmatrix}. \tag{28c}$$

where $\underline{\underline{M}}_{11} = \hat{\underline{\mathfrak{b}}}_1 \underline{\underline{M}}\, \hat{\underline{\mathfrak{b}}}_1^T$, $\underline{\underline{M}}_{12} = \hat{\underline{\mathfrak{b}}}_1 \underline{\underline{M}}\, \hat{\underline{\mathfrak{b}}}_2^T$, $\underline{\underline{M}}_{22} = \hat{\underline{\mathfrak{b}}}_2 \underline{\underline{M}}\, \hat{\underline{\mathfrak{b}}}_2^T$, $\underline{\underline{C}}_1 = \underline{\underline{C}}\, \hat{\underline{\mathfrak{b}}}_1^T$, and $\underline{\underline{C}}_2 = \underline{\underline{C}}\, \hat{\underline{\mathfrak{b}}}_2^T$. Matrices $\breve{\underline{\underline{M}}}_{11}$, $\breve{\underline{\underline{M}}}_{12}$, $\breve{\underline{\underline{M}}}_{22}$, and $\breve{\underline{\underline{E}}}$ are symmetric whereas matrices $\breve{\underline{\underline{H}}}_1$ and $\breve{\underline{\underline{H}}}_2$ are skew-symmetric. By construction, the first $3N$ equations of system (26) are the local equilibrium equations of the problem and the last eight define the stress resultant as per equation (21). The first $3N$ equations also imply global equilibrium. Indeed, multiplication of system (26) by $[\underline{\underline{Z}}^T, \underline{\underline{0}}]$ yield the global equilibrium equations (24). Consequently, system (26) is solvable only for the stress resultants that satisfy the global equilibrium equations.

The vanishing of the coefficients of the virtual displacement field, $\underline{\delta \mathcal{U}}^*$ and $\delta \underline{\hat{w}}$, along boundary Γ yields the boundary conditions

$$\underline{\hat{P}}_n = \underline{\bar{P}}, \tag{29a}$$

$$\underline{\mathcal{F}}^*_n = \underline{\bar{\mathcal{F}}}^*. \tag{29b}$$

Clearly, local boundary condition (29a) and global boundary condition (29b) are also not independent; left-multiplying of the eq. (29a) yields eq. (29b). In the single-layer plate theory, only the global boundary condition is enforced.

4 Dimensional reduction

The previous section has derived the governing equations for plates from three-dimensional elasticity directly. Rather than using a numerical approach, power series solutions of the problem will be obtained in a recursive manner.

4.1 Power series expansion

The stress resultants will be expanded in power series as

$$\underline{\mathcal{F}}^* = \sum_{k=0}^{\mathcal{O}} \sum_{m+n=k}^{k} \beta_{m,n}^{(k)} \underline{\mathcal{F}}_{m,n}^{(k)} = \sum_{k=0}^{\mathcal{O}} \beta_{m,n}^{(k)} \underline{\mathcal{F}}_{m,n}^{(k)}, \tag{30}$$

where $\mathcal{O}$ indicates the order of the series expansion and $\beta_{m,n}^{(k)} = \eta_1^m \eta_2^n/(m!\,n!)$ are the monomials of the expansion. The second equality defines a simplified notational convention that implies the summation over all values of indices m and n such that $m+n=k$, starting from $m=k$, $n=0$. For the zeroth order, eq. (30) reduces to $\underline{\mathcal{F}}^* = \underline{\mathcal{F}}_{0,0}^{(0)}$, where array $\underline{\mathcal{F}}_{0,0}^{(0)}$ stores the stress resultants at $\eta_1 = \eta_2 = 0$. For the first order, $\underline{\mathcal{F}}^* = \underline{\mathcal{F}}_{0,0}^{(0)} + \eta_1 \underline{\mathcal{F}}_{1,0}^{(1)} + \eta_2 \underline{\mathcal{F}}_{0,1}^{(1)}$, where arrays $\underline{\mathcal{F}}_{1,0}^{(1)}$ and $\underline{\mathcal{F}}_{0,1}^{(1)}$ store stress resultant gradients along unit vectors $\bar{b}_1$ and $\bar{b}_2$, respectively, at the same location. A total number of $N_f = 4(\mathcal{O}+1)(\mathcal{O}+2)$ stress resultant coefficients appear in the expansion.

Array $\underline{\mathbb{F}}$, of size N_f, collects all the coefficients of the expansion as $\underline{\mathbb{F}}^T = \{\underline{\mathcal{F}}_{0,0}^{(0)T}, \underline{\mathcal{F}}_{1,0}^{(1)T}, \underline{\mathcal{F}}_{0,1}^{(1)T}, \ldots\}$, up to order $\mathcal{O}$. For uniformity with subsequent developments, eq. (30) is recast as

$$\underline{\mathcal{F}}^* = \sum_{k=0}^{\mathcal{O}} \beta_{m,n}^{(k)} \underline{\underline{I}}_{m,n}^{(k)} \underline{\mathbb{F}}, \tag{31}$$

where all entries of matrix $\underline{\underline{I}}_{m,n}^{(k)}$, of size $8 \times N_{\mathcal{O}}$, vanish, except for an identity matrix, $\underline{\underline{I}}_{8\times 8}$, such that $\underline{\mathcal{F}}_{m,n}^{(k)} = \underline{\underline{I}}_{m,n}^{(k)} \underline{\mathbb{F}}$. The right-hand side of system (26) is now expanded as

$$\underline{\mathcal{Q}} = \sum_{k=0}^{\mathcal{O}} \beta_{m,n}^{(k)} \underline{\underline{F}}_{m,n}^{(k)} \underline{\mathbb{F}} + \sum_{k=0}^{\mathcal{O}} \beta_{m,n}^{(k)} \underline{\underline{Q}}_{m,n}^{(k)} \underline{\mathbb{Q}}, \tag{32}$$

where the first and second terms correspond to the series expansions of the stress resultants ($\underline{\underline{F}}_{m,n}^{(k)T} = [\underline{\underline{0}}^T, \underline{\underline{I}}_{m,n}^{(k)T}]$) and externally applied loading ($\underline{\underline{Q}}_{m,n}^{(k)T} = [\underline{\underline{I}}_{m,n}^{(k)T}, \underline{\underline{0}}]$), respectively.

4.2 Global equilibrium equations

The combined governing eqs. (26) are solvable for stress resultants that are in equilibrium only, but expansion (31) does not satisfy this requirement. Indeed, introducing this expansion into the global equilibrium eqs. (24) yields a set of algebraic equations,

$$\underline{\underline{\Pi}}\,\underline{\mathbb{F}} = -\underline{\mathbb{A}}, \tag{33}$$

where matrix $\underline{\underline{\Pi}}$ and array $\underline{\mathbb{A}}$ are defined as follows

$$\underline{\underline{\Pi}} = \begin{bmatrix} -\tilde{\mathcal{K}}^{*T} & \underline{\underline{t}}_1 & \underline{\underline{t}}_2 \\ \underline{\underline{0}} & -\mathcal{K}^{*T} & \underline{\underline{0}} \\ \underline{\underline{0}} & \underline{\underline{0}} & -\mathcal{K}^{*T} \end{bmatrix}, \quad \text{and} \quad \underline{\mathbb{A}} = -\begin{Bmatrix} \underline{A}_{0,0}^{(0)} \\ \underline{A}_{1,0}^{(1)} \\ \underline{A}_{0,1}^{(1)} \end{Bmatrix}. \tag{34}$$

Therein the combined curvature tensor is defined as $\underline{\underline{\mathcal{K}}}^* = \underline{\underline{t}}_1^T \tilde{\mathcal{K}}_1^* + \underline{\underline{t}}_2^T \tilde{\mathcal{K}}_2^*$. Array $\underline{\mathbb{A}}$ stores the coefficients of the series expansion of the resultant of the externally applied loads, $\underline{\mathcal{A}}$. For conciseness, the above expressions are written for $\mathcal{O}=1$. In general, matrix $\underline{\underline{\Pi}}$ and array $\underline{\mathbb{A}}$ are of size $N_e \times N_f$, where $N_e = 3(\mathcal{O}+1)(\mathcal{O}+2)$, and $N_e \times 1$, respectively.

Because matrix $\underline{\underline{\Pi}}$ is of rank $N_r = 5\mathcal{O}(\mathcal{O}+1)/2 + (\mathcal{O}+2)$, system (33) imposes conditions on arrays $\underline{\mathbb{F}}$ and $\underline{\mathbb{A}}$. First, the solvability condition of system (33) is $\underline{\underline{N}}^T \underline{\mathbb{A}} = \underline{0}$, where $\underline{\underline{N}}$, of size $N_e \times (N_e - N_r)$, is the null space of Π^T. This imposes $(N_e - N_r)$ conditions on the N_e entries of array $\underline{\mathbb{A}}$, leaving N_r independent coefficients, stored in array $\underline{\alpha}$, and $\underline{\mathbb{A}} = \underline{\underline{\Omega}}\,\underline{\alpha}$. Next, in the absence of externally applied loads, $\underline{\underline{\Pi}}\,\underline{\mathbb{F}} = \underline{0}$, and $\underline{\mathbb{F}}$ must span the null space of $\underline{\underline{\Pi}}$, which is of size $N_f \times (N_f - N_r)$. Hence, $\underline{\mathbb{F}}$ can be expressed in terms of $N_i = N_f - N_r$ independent coefficients, stored in array $\underline{\theta}$, and $\underline{\mathbb{F}} = \underline{\underline{\Lambda}}\,\underline{\theta}$. The complete solution of system (33) is now $\underline{\mathbb{F}} = \underline{\underline{\Lambda}}\,\underline{\theta} + \underline{\underline{\Gamma}}\,\underline{\alpha}$.

For later developments, it is convenient to select the eight first entries of array $\underline{\theta}$ as the stress resultants, $\underline{\mathcal{F}}^{(0)}_{0,0}$; the remaining entries correspond to stress resultant derivatives. Matrix $\underline{\underline{\Lambda}}$ then presents the following structure

$$\underline{\underline{\Lambda}}_{N_f \times N_i} = \begin{bmatrix} \underline{\underline{I}}_{8\times 8} & \underline{\underline{0}} \\ \underline{\underline{\Upsilon}} & \underline{\underline{\Xi}} \end{bmatrix}. \tag{35}$$

Although not uniquely defined, Boolean matrices $\underline{\underline{\Upsilon}}$, $\underline{\underline{\Xi}}$, and $\underline{\underline{\Gamma}}_{N_f \times N_r}$ can be obtained from symbolic manipulation programs easily for specific choices of the independent parameters.

It the stress resultant coefficients, $\underline{\mathbb{F}}$, are obtained numerically, for instance from a finite element code solving plate problems, system (33) will not be satisfied exactly. The stress resultant coefficients can then be corrected, in a least squares sense, to enforce the exact satisfaction of this system. The highest-order equilibrium equations suffer from a truncation error: for the $\mathcal{O} = 1$ case illustrated in eq. (34), $\tilde{\mathcal{K}}^{*T}\underline{\mathcal{F}}^{(1)}_{1,0} = \underline{A}^{(1)}_{1,0}$ and $\tilde{\mathcal{K}}^{*T}\underline{\mathcal{F}}^{(1)}_{0,1} = \underline{A}^{(1)}_{0,1}$. For the unloaded case, these imply the vanishing of the first derivatives of the shear force components, which instead, should be related to the second derivatives of the stress resultants, if not for the truncated expansion. To remedy this shortcoming, corrective loading resultants are evaluated as $\underline{A}^{(1)}_{1,0} = \underline{\underline{Z}}^T\underline{Q}^{(1)}_{1,0} = \tilde{\mathcal{K}}^{*T}\underline{\mathcal{F}}^{(1)}_{1,0}$ and applied to the plate as distributed loads, $\underline{Q}^{(1)}_{1,0} = \underline{\underline{Z}}(\underline{\underline{Z}}^T\underline{\underline{Z}})^{-1}\tilde{\mathcal{K}}^{*T}\underline{\mathcal{F}}^{(1)}_{1,0}$. Of course, this correction is applied to the highest order only.

4.3 The series solution

The unloaded plate problem, *i.e.,* $\underline{Q} = \underline{0}$, is considered first. Particular solutions of system (26) are obtained by assuming the solution array to be expanded in power series, $\underline{\mathcal{X}} = \sum_{k=0}^{\mathcal{O}} \beta^{(k)}_{m,n}\underline{\underline{X}}^{(k)}_{m,n}\underline{\mathbb{F}}$, where $\underline{\underline{X}}^{(k)T}_{m,n} = [\underline{\underline{W}}^{(k)T}_{m,n}, \underline{\bar{S}}^{*(k)T}_{m,n}]$, and matching the coefficients of the monomials. Because array $\underline{\theta}$ is arbitrary, the following recursive equations are obtained

$$\breve{\underline{\underline{E}}}\,\underline{\underline{X}}^{(\mathcal{O})}_{m,n} = \underline{\underline{F}}^{(\mathcal{O})}_{m,n}, \tag{36a}$$

$$\breve{\underline{\underline{E}}}\,\underline{\underline{X}}^{(\mathcal{O}-1)}_{m,n} = \underline{\underline{F}}^{(\mathcal{O}-1)}_{m,n} + \breve{\underline{\underline{H}}}_1\underline{\underline{X}}^{(\mathcal{O})}_{m+1,n} + \breve{\underline{\underline{H}}}_2\underline{\underline{X}}^{(\mathcal{O})}_{m,n+1}, \tag{36b}$$

$$\begin{aligned}\breve{\underline{\underline{E}}}\,\underline{\underline{X}}^{(k)}_{m,n} = {} & \underline{\underline{F}}^{(k)}_{m,n} + \breve{\underline{\underline{H}}}_1\underline{\underline{X}}^{(k+1)}_{m+1,n} + \breve{\underline{\underline{H}}}_2\underline{\underline{X}}^{(k+1)}_{m,n+1} \\ & + \breve{\underline{\underline{M}}}_{11}\underline{\underline{X}}^{(k+2)}_{m+2,n} + \breve{\underline{\underline{M}}}_{12}\underline{\underline{X}}^{(k+2)}_{m+1,n+1} + \breve{\underline{\underline{M}}}_{22}\underline{\underline{X}}^{(k+2)}_{m,n+2}.\end{aligned} \tag{36c}$$

For simplicity, matrix $\underline{\underline{\Lambda}}$ that multiplies each term of these equations was omitted. Note the recursive nature of the equations where the solutions of systems (36a) appear on the right-hand side of systems (36b), etc. Equations (36a) and (36b) represent $\mathcal{O}+1$ and $\mathcal{O}$ independent linear systems, respectively, for the values of indices m and n such that $m+n = \mathcal{O}$ and $m+n = \mathcal{O}-1$, respectively. Equations (36c) are valid for $k = 0, 1, \ldots, \mathcal{O}-2$; each equations represents a total of $k+1$ linear systems for $m+n = k$. Because the stress resultants are in equilibrium, it is proved easily that the solvability conditions are satisfied for each of the systems (36). More details about the solution process are given in B.

The nodal forces defined by eq. (17) can be expressed as $\underline{\hat{P}} = \sum_{k=0}^{\mathcal{O}} \beta^{(k)}_{m,n}\underline{\underline{Y}}^{(k)}_{m,n}\underline{\mathbb{F}}$, where matrices $\underline{\underline{Y}}^{(k)}_{m,n}$ are defined as

$$\underline{\underline{Y}}^{(k)}_{m,n} = \underline{\underline{M}}\,\underline{\underline{J}}^{(k)}_{m,n} + \underline{\underline{C}}^T\underline{\underline{W}}^{(k)}_{m,n}, \tag{37}$$

and matrices $\underline{\underline{J}}^{(k)}_{m,n}$ as

$$\underline{\underline{J}}^{(\mathcal{O})}_{m,n} = \underline{\underline{G}}\,\underline{\underline{\mathcal{S}}}^{*(\mathcal{O})}_{m,n}, \tag{38a}$$

$$\underline{\underline{J}}^{(k)}_{m,n} = \underline{\underline{G}}\,\underline{\underline{\mathcal{S}}}^{*(k)}_{m,n} + \hat{\underline{\underline{\mathfrak{b}}}}^T_1\underline{\underline{W}}^{(k+1)}_{m+1,n} + \hat{\underline{\underline{\mathfrak{b}}}}^T_2\underline{\underline{W}}^{(k+1)}_{m,n+1}, \tag{38b}$$

where eq. (38b) holds for $k = 0, 1, \ldots, \mathcal{O}-1$.

The first $3N$ equations of each of systems (36) can be recast in the following form

$$\underline{\underline{E}}\,\underline{\underline{W}}^{(\mathcal{O})}_{m,n} = -\underline{\underline{C}}\,\underline{\underline{J}}^{(\mathcal{O})}_{m,n}, \tag{39a}$$

$$\underline{\underline{E}}\,\underline{\underline{W}}^{(k)}_{m,n} = -\underline{\underline{C}}\,\underline{\underline{J}}^{(k)}_{m,n} + \hat{\underline{\underline{\mathfrak{b}}}}_1\underline{\underline{Y}}^{(k+1)}_{m+1,n} + \hat{\underline{\underline{\mathfrak{b}}}}_2\underline{\underline{Y}}^{(k+1)}_{m,n+1}, \tag{39b}$$

where eq. (39b) holds for $k = 0, 1, \ldots, \mathcal{O}-1$. Factorizing $\underline{\underline{G}}^T$ in the last eight equations of each of systems (36) yields the following relationships

$$\underline{\underline{G}}^T\underline{\underline{Y}}^{(k)}_{m,n} = \underline{\underline{F}}^{(k)}_{m,n}. \tag{40}$$

4.4 Global compliance matrix

Once the series solution of the combined equations has been found through the recursive solution of eqs. (36), the associated local strain components can be recovered from eq. (13). Evaluating the local strains at $\eta_1 = \eta_2 = 0$ leads to

$$\underline{\gamma}^*_0 = \left[(\underline{\underline{A}}\,\underline{\underline{N}}) \quad (\underline{\underline{B}}\,\underline{\underline{N}})\right]\underline{\underline{\mathcal{L}}}^*_0\mathbb{F}, \tag{41}$$

where matrix $\underline{\underline{\mathcal{L}}}^*_0$ stores the nodal displacements derivatives, $\underline{\underline{J}}^{(0)}_{0,0}$, and nodal warping, $\underline{\underline{W}}^{(0)}_{0,0}$,

$$\underline{\underline{\mathcal{L}}}^*_0 = \begin{bmatrix} \underline{\underline{J}}^{(0)}_{0,0} \\ \underline{\underline{W}}^{(0)}_{0,0} \end{bmatrix}. \tag{42}$$

The global compliance matrix is obtained by evaluating the strain energy stored in the three-dimensional structure. Introducing the local strain distribution (41) into the strain energy density, $\mathfrak{a}$, and integrating through the thickness of the plate yields

$$\mathfrak{a} = \frac{1}{2}\underline{\theta}^T\underline{\underline{\mathbb{S}}}^*\underline{\theta}, \tag{43}$$

where $\underline{\underline{\mathbb{S}}}^*$ is the positive-definite, symmetric, global compliance matrix of the plate,

$$\underline{\underline{\mathbb{S}}}^* = (\underline{\underline{\mathcal{L}}}^*_0\underline{\underline{\Lambda}})^T\begin{bmatrix} \underline{\underline{M}} & \underline{\underline{C}}^T \\ \underline{\underline{C}} & \underline{\underline{E}} \end{bmatrix}(\underline{\underline{\mathcal{L}}}^*_0\underline{\underline{\Lambda}}). \tag{44}$$

The global compliance matrix is of size $N_i \times N_i$, *i.e.*, depends on the order of the series expansion. Within the discretization and truncation errors, the strain energy computed by eq. (43) equals that computed in the local model exactly because it is obtained through integration of the local strain distribution. Clearly, the strain energy depends on the stress resultants (the first eight entries of array $\underline{\theta}$) but also on their spatial derivatives (the remaining entries of array $\underline{\theta}$). For higher-order series expansions, the strain energy depends on increasingly higher-order derivatives of the stress resultants.

Because they are based on the rigid-normal assumption, the Reissner-Mindlin plate theories involve 8×8 compliance matrices that defines the strain energy per unit area of the plate as $\mathfrak{a} = 1/2\ \underline{\mathcal{F}}^{*T}\underline{\underline{\mathcal{S}}}^*_{RM}\underline{\mathcal{F}}^*$, where $\underline{\underline{\mathcal{S}}}^*_{RM} = \underline{\underline{\mathcal{C}}}^{*-1}_{RM}$, *i.e.*, the strain energy density is a function of the eight stress resultants only. In contrast, because the present approach is derived from three-dimensional elasticity without a priori kinematic assumptions, the resulting strain energy density depends on the stress resultants and their spatial derivatives.

This discussion leads to the following question: can the strain energy density of the proposed approach be expressed, although approximately, in terms of stress resultants only? The first eight

entries of array $\underline{\theta}$ are the stress resultants, the remaining entries are spatial derivatives of these quantities. Intuitively, for plate problems, spatial derivatives of the stress resultants should be far smaller than the stress resultants themselves. Indeed, if this condition is not satisfied, high stress gradients result and the problem should be treated as a genuine problem of three-dimensional elasticity, not as a plate problem. Consequently, the following should hold,

$$\mathfrak{a} \approx \frac{1}{2}\underline{\mathcal{F}}^{*T}\underline{\underline{\mathcal{S}}}^{*}_{\mathrm{rd}}\underline{\mathcal{F}}^{*}, \tag{45}$$

where the reduced compliance matrix, $\underline{\underline{\mathcal{S}}}^{*}_{\mathrm{rd}}$, stores the first 8×8 entries of matrix $\underline{\underline{\mathbb{S}}}^{*}$. Although of reduced size, this compliance matrix takes into account warping deformations, in contrast with the Reissner-Mindlin compliance matrix, $\underline{\underline{\mathcal{S}}}^{*}_{RM}$, which does not.

Given the special structure of matrix $\underline{\underline{\Lambda}}$ expressed by eq. (35), it can be shown that the reduced compliance matrix, $\underline{\underline{\mathcal{S}}}^{*}_{\mathrm{rd}}$, becomes independent of the order of the expansion for $\mathcal{O} >= 1$. Because this matrix captures the plate's strain energy density more accurately than that derived from Reissner-Mindlin theories, the preferred expression for this strain energy density is $\mathfrak{a} = 1/2\ \underline{\mathcal{F}}^{*T}\underline{\underline{\mathcal{S}}}^{*}_{\mathrm{rd}}\underline{\mathcal{F}}^{*}$.

Once the sectional compliance $\underline{\underline{\mathbb{S}}}^{*}$ is determined, the governing equations of single-layer model are closed: the equivalent two-dimensional problem reduces to the solution of the constitutive relation $\underline{\mathcal{E}}^{*} = \underline{\underline{\mathbb{S}}}^{*}\underline{\mathcal{F}}^{*}$, equilibrium equations (24), strain-displacement relationships (9), and boundary conditions (29b).

5 Stress recovery

The previous section has focused on the determination of the plate's stiffness matrix. The attention now turns to the recovery of the local stress and strain fields, which depend on the details of the applied loading. Hence, the right-hand side of system (26) must now include all applied loads and their power series expansion given by eq. (32). The solution procedure is based on a recursive process similar to that described in the previous section; details are omitted. The local strain components, defined in (41), are $\underline{\gamma}^{*} = [\underline{\underline{A}}\,\underline{\underline{N}}\ \ \underline{\underline{B}}\,\underline{\underline{N}}]\ \underline{\mathcal{L}}^{*}_{0}$. Once local strains are recovered, local stresses follows from the constitutive laws.

As discussed in sec. 3.4, system (26) is solvable only when the global equilibrium equations are satisfied. In practice, the stress resultants are obtained from the numerical solution of the plate equations, using a finite element approximation, for instance. In such case, a least squares process is used to correct the stress resultants and their spatial derivatives to ensure strict satisfaction of the global equilibrium equations.

6 Numerical results

To validate the dimensional reduction and stress recovery analysis procedures proposed in this paper, a set of numerical examples will be presented.

6.1 Cylindrical bending problem

This example focuses on a laminated composite plate of width L and thickness $h = L/4$ undergoing cylindrical bending, as depicted in fig. 3. The plate is of infinite length along unit vector $\bar{\imath}_2$ and is simply supported along the two opposite edges at $\eta_1 = 0$ and L. The plate is subjected to distributed transverse pressures $p_t(\eta_1) = p_b(\eta_1) = p_0/2\sin(\pi\eta_1/L)$ over both top and bottom surfaces (For clarity, fig. 3 only shows the loading acting over the top surface). The following lay-up configurations are investigated, case (a): a four layer lay-up, $[15^{\circ}_2, -15^{\circ}_2]$, case (b): a four layer

lay-up, $[30°, -30°_2, 30°]$, case (c): a ten layer lay-up $[10°, 30°_2, 60°, 45°, -45°, -20°_2, 60°, 10°]$; all plies are of equal thickness and description of the stacking sequences starts from the bottom ply. The following sign conventions are used: 0° fibers are aligned with unit vector $\bar{\imath}_1$ and a positive ply angle indicates a right-hand rotation about unit vector $\bar{\imath}_3$. All layers are made of the same material with the following physical properties: longitudinal, transverse, and shear moduli are $E_L/E_T = 25$, $G_{LT}/E_T = 0.5$, and $G_{TT}/E_T = 0.2$, respectively; Poisson's ratios are $\nu_{LT} = \nu_{TN} = 0.25$. The stiffness parameters are non-dimensionalized with respect to transverse modulus E_T.

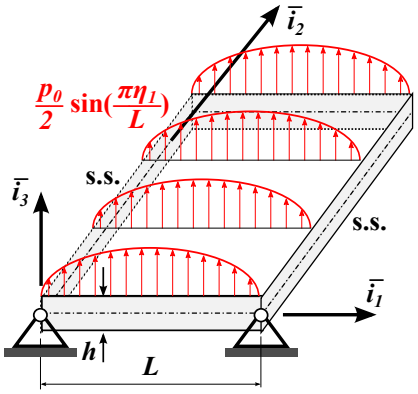

Figure 3: Configuration of the cylindrical bending problem.

In the proposed approach, a single four-node one-dimensional element was used to model each ply and the investigation focuses on the stress recovery process. The predictions of three expansion orders, constant, linear, and quadratic were compared to assess the accuracy and convergence of the proposed approach. Pagano [33] obtained an analytical solution of this problem and exact stress resultants and their derivatives were obtained by integrating the exact three-dimensional stress distribution through the plate's thickness.

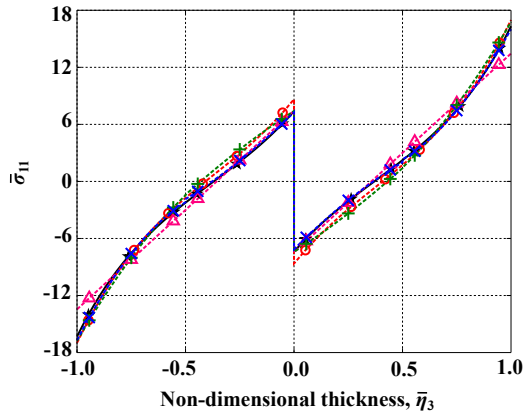

Figure 4: Distribution of stress component $\bar{\sigma}_{11}$ through the thickness, case (a).

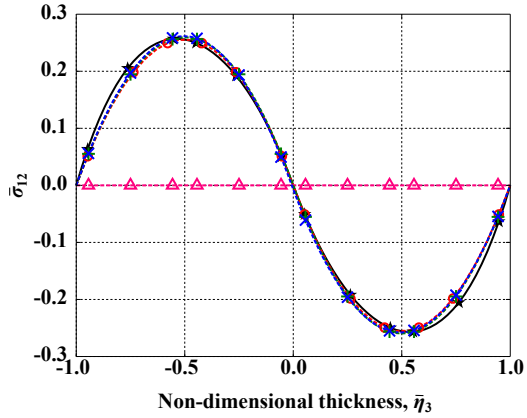

Figure 5: Distribution of stress component $\bar{\sigma}_{12}$ through the thickness, case (a).

The distributions of the non-dimensional stress components, $\bar{\sigma}_{ij} = \sigma_{ij}/p_0$, through the thickness of the plate were evaluated for cases (a), (b) and (c). Figure 4 and 5 show the distribution of in-plane stress component, $\bar{\sigma}_{11}$ and $\bar{\sigma}_{12}$, respectively, through the thickness of the plate for case (a). In these figures, predictions for $\mathcal{O}$= 0, 1, and 2 are indicated with symbols $\triangle$, $+$, and $\times$, respectively, while symbol $\star$ indicates the exact solution of Pagano [33]. When available, the solutions obtained from of the Variational Asymptotic Plate And Shell Analysis [27, 28] (VAPAS) are indicated by symbol $\circ$. VAPAS used a second-order series expansion of the plate's sectional strains. The predictions of the proposed approach are in excellent agreement with those of the exact solution for $\mathcal{O} \geq 1$. The corresponding results for cases (b) and (c) are presented in figs. 6, 7 and figs 8, 9, respectively.

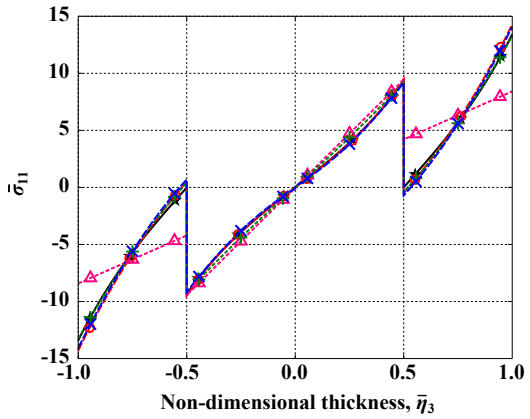

Figure 6: Distribution of stress component $\bar{\sigma}_{11}$ through the thickness, case (b).

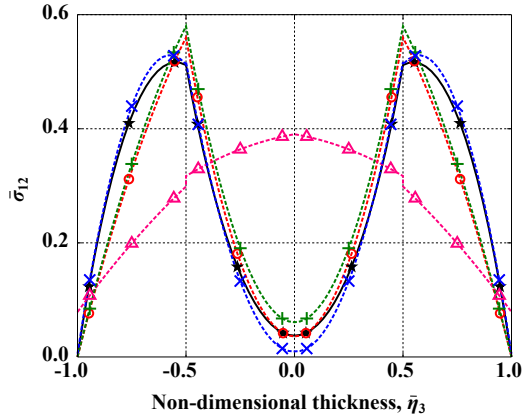

Figure 7: Distribution of stress component $\bar{\sigma}_{12}$ through the thickness, case (b).

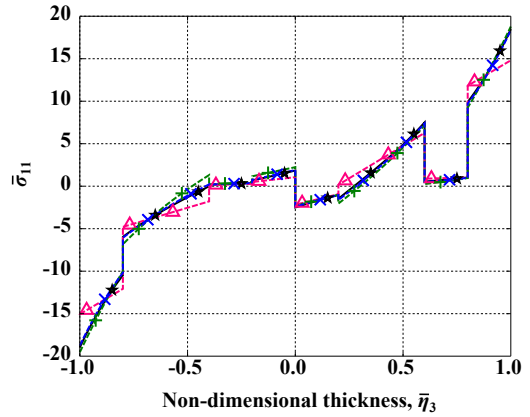

Figure 8: Distribution of stress component $\bar{\sigma}_{11}$ through the thickness, case (c).

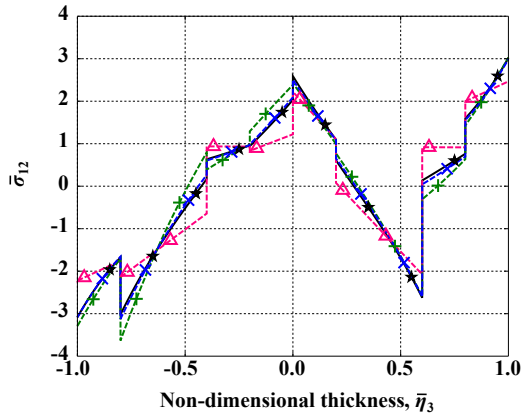

Figure 9: Distribution of stress component $\bar{\sigma}_{12}$ through the thickness, case (c).

Finally, the interlaminar shear stress components $\bar{\sigma}_{13}$ and $\bar{\sigma}_{23}$ are shown in figs. 10 to 13, respectively. For all the lay-up configurations, the predictions of the proposed approach are in excellent agreement with the analytical solutions as $\mathcal{O} \geq 1$.

The predictions for the ten-layer plate are as accurate as those for four-layer plate. Because both three-dimensional equilibrium and interlaminar compatibility equations are satisfied rigorously in the proposed approach, the accuracy of the solution is independent of the number of layers. As long as the stress gradients in the midplane surface are small, stresses can be recovered accurately.

6.2 Spatial bending problem

The square laminated composite plate of size $L \times L$ and thickness $h = L/10$ depicted in fig. 14 undergoes spatial bending. The plate is simply supported along all four edges and is subjected to distributed transverse pressures $p_t(\eta_1, \eta_2) = p_b(\eta_1, \eta_2) = p_0/2 \sin(\pi\eta_1/L) \sin(\pi\eta_2/L)$ over both top and bottom surfaces (For clarity, fig. 14 only shows the loading acting over the top surface). The plate consist of 4 plies, each of thickness $t_p = h/4$. All four plies are made of the same material with the following stiffness properties: longitudinal and shear moduli are $E_L/E_T = 25$, $G_{LT}/E_T = 0.5$, and $G_{TT}/E_T = 0.2$, respectively; Poisson's ratios are $\nu_{LT} = \nu_{TN} = 0.25$.

The lay-up configuration investigated here presents the following stacking sequence, $[0°, 90°_2, 0°]$; $0°$ fibers are aligned with unit vector $\bar{\imath}_1$ and a positive ply angle indicates a right-hand rotation about unit vector $\bar{\imath}_3$.

In the proposed approach, a single four-node one-dimensional element was used to model each

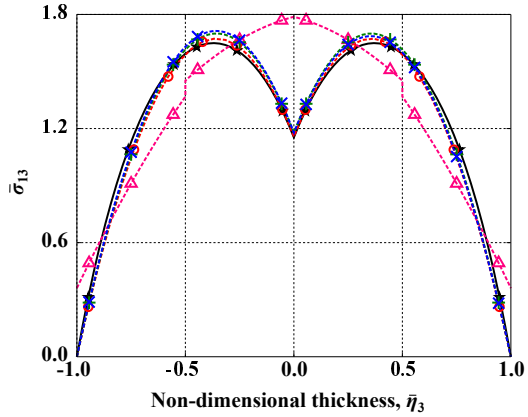

Figure 10: Distribution stress component, $\bar{\sigma}_{13}$, for case (a).

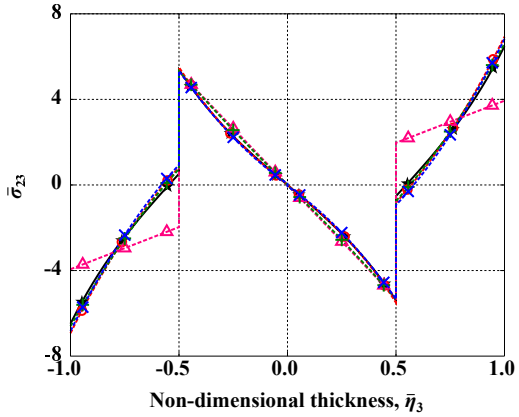

Figure 11: Distribution stress component, $\bar{\sigma}_{23}$, for case (b).

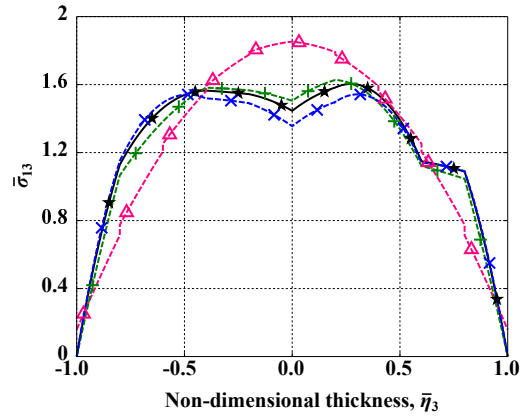

Figure 12: Distribution stress component, $\bar{\sigma}_{13}$, for case (c).

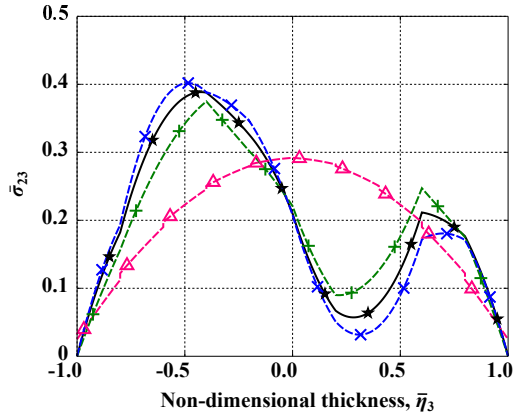

Figure 13: Distribution stress component, $\bar{\sigma}_{23}$, for case (c).

ply. Because the lay-up is symmetric through the plate's thickness, only three sub-matrices of the complete 8×8 reduced stiffness matrix, $\underline{\underline{\mathcal{S}}}^*_{\text{rd}}$, do not vanish: the 3×3 in-plane, 2×2 shearing, and 3×3 bending stiffness matrices, denoted $\underline{\underline{A}}_{\text{rd}}$, $\underline{\underline{S}}_{\text{rd}}$, and $\underline{\underline{D}}_{\text{rd}}$, respectively. The same holds for the stiffness matrix obtained from the Reissner-Mindlin theory, denoted $\underline{\underline{\mathcal{C}}}^*_{RM}$. The in-plane stiffness matrices predicted by the two approaches are

$$\frac{\underline{\underline{A}}_{\text{rd}}}{E_T L} = \begin{bmatrix} 1.303 & 0.025 & 0.0 \\ 0.025 & 1.303 & 0.0 \\ 0.0 & 0.0 & 0.050 \end{bmatrix}, \quad \frac{\underline{\underline{A}}_{RM}}{E_T L} = \begin{bmatrix} 1.312 & 0.0336 & 0.0 \\ 0.0336 & 1.312 & 0.0 \\ 0.0 & 0.0 & 0.050 \end{bmatrix}. \tag{46}$$

While the two matrices differ, it is clear that the warping induced deformations taken into account by the present approach have minimal effect on the in-plane stiffness matrix. Although the

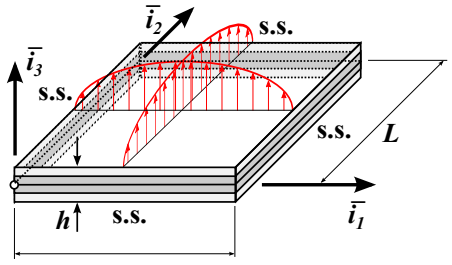

Figure 14: Configuration of the spatial bending problem.

discrepancies are larger, the same observations apply to the bending stiffness matrix,

$$\frac{\underline{\underline{D}}_{\text{rd}}}{10^{-6}E_T L^3} = \begin{bmatrix} 334.2 & -20.9 & 0.0 \\ -20.9 & 1838 & 0.0 \\ 0.0 & 0.0 & 41.7 \end{bmatrix}, \quad \frac{\underline{\underline{D}}_{RM}}{10^{-6}E_T L^3} = \begin{bmatrix} 340.3 & -28.0 & 0.0 \\ -28.0 & 1846 & 0.0 \\ 0.0 & 0.0 & 41.7 \end{bmatrix}. \tag{47}$$

Finally, the same warping deformations affect the shearing stiffness matrix drastically,

$$\frac{\underline{\underline{S}}_{\text{rd}}}{10^{-2}E_T L} = \begin{bmatrix} 1.903 & 0.0 \\ 0.0 & 3.179 \end{bmatrix}, \quad \frac{\underline{\underline{S}}_{RM}}{10^{-2}E_T L} = \begin{bmatrix} 3.500 & 0.0 \\ 0.0 & 3.500 \end{bmatrix}. \tag{48}$$

As expected, warping induced deformations reduce the plate's effective stiffness.

Because the configuration of the present problem is simple, Navier type solutions [1, 2] can be found easily with a single sine-wave term only. Such solutions were obtained based on two stiffness matrices: the reduced stiffness matrix of the proposed approach, $\underline{\underline{\mathcal{C}}}^*_{\text{rd}}$, and that of Reissner-Mindlin theory, $\underline{\underline{\mathcal{C}}}^*_{\text{RM}}$. Table 1 lists the maximum values of the stress resultants and the mid-point vertical displacement for these two cases. Clearly, the predictions based on the proposed stiffness matrix are in closer agreement with the exact solution than those based on the classical, Reissner-Mindlin stiffness matrix.

	Exact	Navier, $\underline{\underline{\mathcal{C}}}^*_{\text{rd}}$		Navier, $\underline{\underline{\mathcal{C}}}^*_{\text{RM}}$	
		Values	Difference	Values	Difference
Q_1^*/p_0	0.2357	0.2321	1.5 %	0.2448	3.9 %
Q_2^*/p_0	0.0826	0.0863	4.5 %	0.0735	- 11.0 %
$M_1^*/(p_0 L)$	- 0.0221	- 0.0231	4.5 %	- 0.0195	- 11.9 %
$M_2^*/(p_0 L)$	0.0708	0.0695	- 1.8%	0.0740	4.5 %
$M_{12}^*/(p_0 L)$	0.0042	0.0043	2.4 %	0.0039	- 6.4 %
$E_T u_3^*/(p_0 L)$	7.3698	7.6378	3.6 %	6.2235	- 15.6 %

Table 1: Comparing the exact and Navier solutions

In section 4.4, the global compliance matrix was reduced from size $N_i \times N_i$ to 8×8, arguing that the magnitudes of the stress resultant gradients must be far smaller than those of the stress resultants themselves. To verify this claim, the strain energy density at the plate's mid-point was evaluated based on the exact solution of the problem derived by Fan and Ye [34], to find $a = 1/2 \int_{\mathcal{L}} \underline{\gamma}^{*T} \underline{\underline{\mathcal{D}}}^* \underline{\gamma}^* \mathrm{d}\eta_3 = 2.0625\ p_0^2 L/E_T$. Next, the same strain energy was evaluated based on the reduced stiffness matrix, $\underline{\underline{\mathcal{C}}}^*_{\text{rd}}$, and stress resultants of the associated Navier solution, leading to $a = 2.0618\ p_0^2 L/E_T$. Finally, if using the Reissner-Mindlin compliance matrix, $\underline{\underline{\mathcal{C}}}^*_{\text{RM}}$, and stress resultants of the corresponding Navier solution, the same energy becomes, $a = 1.9933\ p_0^2 L/E_T$.

The strain energy predicted by the proposed approach is in close agreement with its exact counterpart: the 0.03% discrepancy is due to discretization and truncation errors. With the Reissner-Mindlin stiffness matrix, the error becomes 3.4%. Clearly, the reduced stiffness predicted by the proposed approach should be used instead of its Reissner-Mindlin counterpart as it captures the strain energy density more accurately.

Next, using the predictions obtained from Navier's solution with the proposed reduced stiffness matrix, the local stress field was evaluated through the thickness of the plate. In the stress recovery process, the predictions of three expansion orders, constant, linear, and quadratic were compared to assess the convergence of the proposed approach.

Figures 15, 16, and 17 depict the through-the-thickness distribution of non-dimensional direct stress components, $\bar{\sigma}_{ii} = \sigma_{ii}/p_0$, $i = 1, 2, 3$. In these figures, the predictions for $\mathcal{O}$= 0, 1, and 2 are

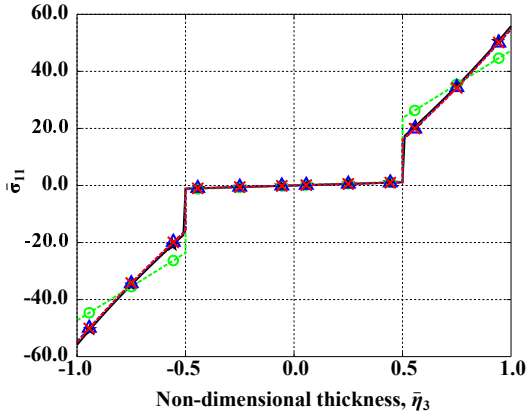

Figure 15: Distribution of stress component $\bar{\sigma}_{11}$ through the plate's thickness.

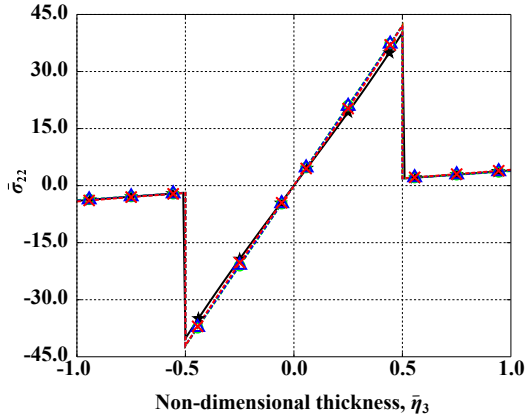

Figure 16: Distribution of stress component $\bar{\sigma}_{22}$ through the plate's thickness.

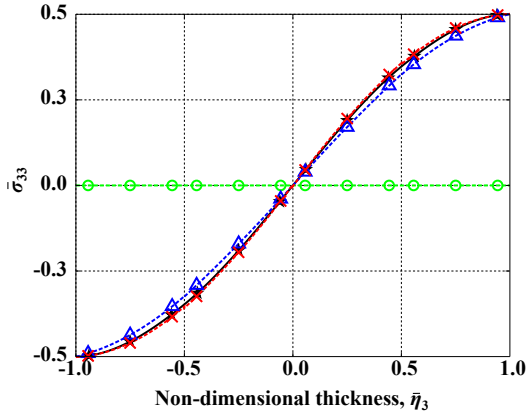

Figure 17: Distribution of stress component $\bar{\sigma}_{33}$ through the plate's thickness.

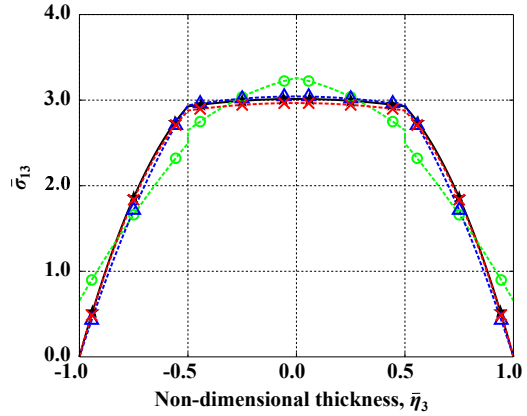

Figure 18: Distribution of stress component $\bar{\sigma}_{13}$ through the plate's thickness.

indicated with symbols $\circ$, $\triangle$, and $\times$, respectively, while the exact solution by Fan and Ye [34] is indicated with symbol $\star$.

The predictions for shear stress components $\bar{\sigma}_{13}$, $\bar{\sigma}_{23}$, and $\bar{\sigma}_{12}$ are shown in figs. 18, 19, and 20, respectively. For the lowest-order expansion, $\mathcal{O} = 0$, the predictions are not accurate while the predictions for $\mathcal{O} = 1$ or 2 are in close agreement with the exact solutions, demonstrating its good convergence characteristics. Although the plate equations were solved using Navier's solution, very accurate stress and stress gradient distributions are recovered through the plate's thickness for $\mathcal{O} \geq 1$.

6.3 Sandwich plate subjected to local pressures

Finally, the attention turns to a sandwich plate subjected to local pressures on its top surface. Analytical solutions for this problem were found by Meyer-Piening [35]. Carrera and Demasi [36] assessed the accuracy of various types of single-layer and layer-wise plate models for this problem. The sandwich plate, of size $a \times b = 100 \times 200$ mm^2, is simply supported along all four edges, and subjected to transverse pressures applied in a small rectangular region, bounded by $(a_1, a_2) = (47.5, 52.5)$ mm and $(b_1, b_2) = (90, 110)$ mm. The harmonic expansion of the pressure loading is

$$p = \sum_{i=1}^{m} \sum_{j=1}^{n} p_{mn} \sin \frac{\pi \eta_1}{m} \sin \frac{\pi \eta_2}{n}, \tag{49}$$

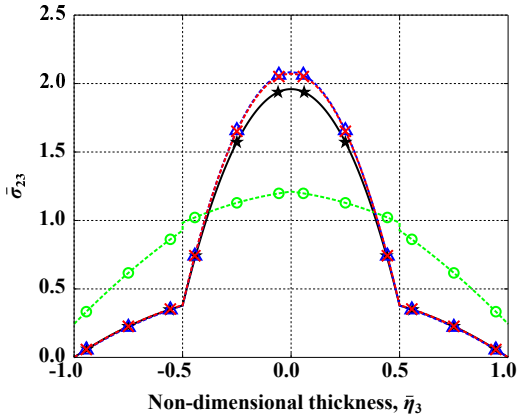

Figure 19: Distribution of stress component $\bar{\sigma}_{23}$ through the plate's thickness.

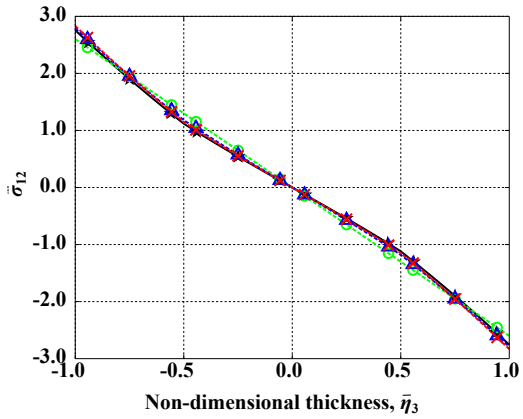

Figure 20: Distribution of stress component $\bar{\sigma}_{12}$ through the plate's thickness.

where the coefficients of the expansion, $p_{m,n}$, are

$$p_{m,n} = \frac{4p}{\pi^2 mn}(\cos\frac{m\pi a_1}{a} - \cos\frac{m\pi a_2}{a})(\cos\frac{n\pi b_1}{b} - \cos\frac{n\pi b_2}{b}). \tag{50}$$

The core, upper, and lower faces are of thicknesses $h_c = 11.4$ mm, $h_t = 0.1$ mm and $h_b = 0.5$ mm, respectively. The upper and lower faces are made of the same orthotropic material with the following stiffness properties: $E_1 = 70$ GPa, $E_2 = 71$ GPa, $E_3 = 69$ GPa, $G_{12} = G_{13} = G_{23} = 26$ GPa, and $\nu_{13} = \nu_{13} = \nu_{23} = 0.3$. The core material is transversely isotropic along the direction of axis $\bar{b}_3$ and its stiffness properties are $E_1 = E_2 = 3$ MPa, $E_3 = 2.8$ MPa, $G_{12} = G_{13} = G_{23} = 1$ MPa, and $\nu_{12} = \nu_{13} = \nu_{23} = 0.25$.

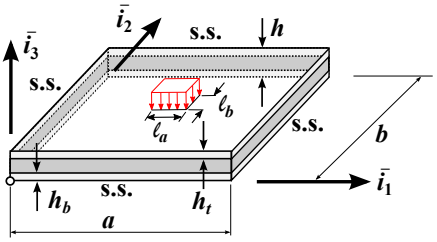

Figure 21: Configurations of the sandwich plate problems.

In the proposed approach, meshes of 1, 1, and 2 four-node one-dimensional element were uswed to model the upper face, lower face, and the core, respectively. Navier type solutions were found easily with the predicted 8×8 sectional stiffness matrix. Next, the local stress field was evaluated through the thickness of the plate based on the stress resultants and their first-order partial derivatives.

The stress components at the center of the plate, $(\eta_1, \eta_2) = (50, 100)$ mm, are listed in table 2. The predicted stress components at the top and bottom locations of the upper face, lower face, and the core are listed for the exact solution given by Meyer-Piening [35], a three-dimensional FEM solution by the same author, the layer-wise theory of Carrera and Demasi [36], and the present approach. The predictions of the proposed approach are not in good agreement with those of the exact solution.

The present approach assumes that the gradients of the stress resultants are far smaller than the stress resultants themselves. Clearly, this assumption is not satisfied here: simple equilibrium arguments shows that the transverse shear forces present a discontinuity at the edge of the loading patch, see fig. 21. In that region, only a truly three-dimensional solution is expected to predict stresses accurately. Because the solution is obtained via Navier's approach, stresses and stress

resultants are expressed as series expansion in terms of the loading harmonics, see eq. (50). Consequently, stress resultant derivatives with respect to η_1 and η_2 are proportional to the squares of wave numbers m and n. Although the magnitude of excitation of each harmonic decreases with increasing wave number, stress resultant gradient increase and the accuracy of the predictions degrades rapidly. Figures 22, 23, 24, and 25 compare the exact (solid line) and present (dashed line) predictions for $m = n = 1$, 2, 3 and 4, respectively. As pointed out by Carrera and Demasi [36], single-layer models fail to predict accurate three-dimensional stresses for this high stress gradient problem; three-dimensional or layer-wise models should be used instead.

Approach	η_3	u_3 (mm)	σ_{11} (MPa)	σ_{22} (MPa)	σ_{12}
	upper face				
Exact [35]	Top	-3.78	-624	-241	0
	Bottom		580	211	0
3D FEM [35]	Top	-3.84	-628	237	0
	Bottom		582	102	0
Layer-wise model [36]	Top	-3.728	-595.56	-223.93	0
	Bottom		556.00	196.37	0
Present	Top	-3.5386	-242.05	-125.43	0
	Bottom		329.81	164.46	0
	lower face				
Exact [35]	Top		-138	-121	0
	Bottom	-2.14	146	127	0
3D FEM [35]	Top		-140	120	0
	Bottom	-2.19	158	127	0
Layer-wise model [36]	Top		-136.20	-118.99	0
	Bottom	-2.1403	144.03	125.00	0
Present	Top		-1458.2	-724.51	0
	Bottom		1451.8	725.23	0

Table 2: Comparing different approaches for the sandwich plate problem, where all the components are evaluated at the center of the point $\eta_1 = 50$ mm and $\eta_2 = 100$ mm.

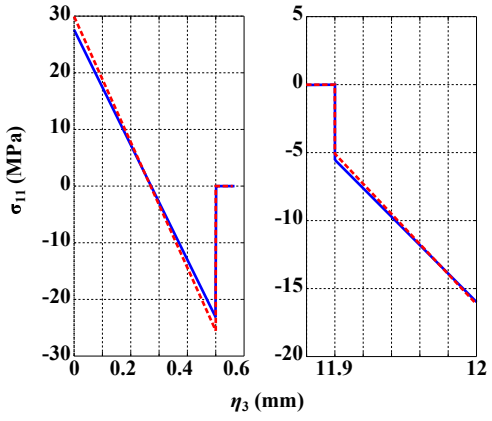

Figure 22: Distribution of stress component σ_{11} through the plate's thickness, $m = 1$, $n = 1$.

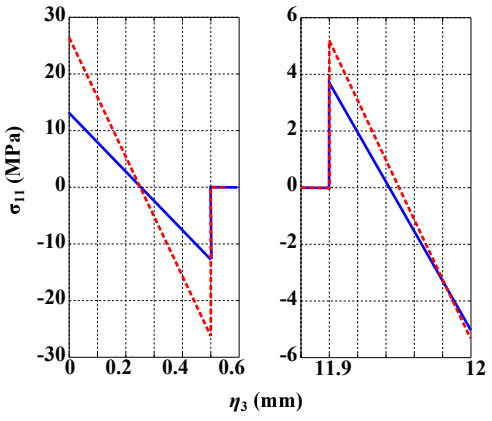

Figure 23: Distribution of stress component σ_{11} through the plate's thickness, $m = 3$, $n = 3$.

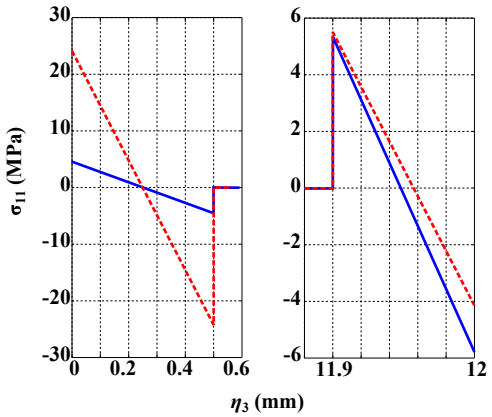

Figure 24: Distribution of stress component σ_{11} through the plate's thickness, $m = 5$, $n = 5$.

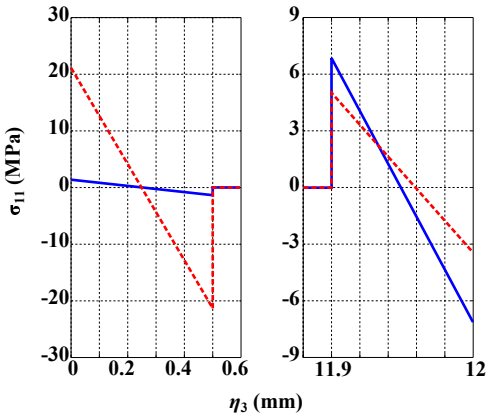

Figure 25: Distribution of stress component σ_{11} through the plate's thickness, $m = 7$, $n = 7$.

7 Conclusions

Based on the assumption of small stress-resultant gradients, a novel, single-layer plate model was developed using local-global modeling. The governing equations for three-dimensional plate problem, combining the equilibrium conditions of both local and global models, were derived from the principle of virtual work. Power series solutions of these equations were found. This rigorous approach to dimensional reduction yields the constitutive laws for the plate and accurate stress distributions through its thickness.

The proposed dimensional reduction process shows that the plate's strain energy density depends on the stress resultants and their spatial derivatives, in contrast with classical plate theories, for which the same strain energy is a function of stress resultants only. For plate problems, spatial derivatives of the stress resultants should be far smaller than the stress resultants themselves. This observation enables the derivation of an 8×8 stiffness matrix for the plate. This stiffness matrix is of the same size as that used in classical plate theories, although its entries differ, because they reflect the plate's warping deformations.

In contrast with higher-order and layer-wise plate theories, the present approach does not increase the number of unknowns. The assumptions associated with commonly used single-layer plate theories have been eliminated altogether. Yet, for problems presenting small stress resultant gradients, the predicted three-dimensional stress distributions through the plate's thickness compare favorably with those predicted by exact elasticity solutions. As stress resultant gradients increase, the accuracy of the predicted three-dimensional stresses deteriorates.

Because it does not increase the number of unknowns, the proposed approach can be used in conjunction with existing plate models, such as those found in commercial finite element packages. It provides an improved, 8×8 stiffness matrix for the plate and furthermore, accurate, through-the-thickness stress distributions can be obtained through a simple post-processing operation. The proposed approach can be generalized to plates undergoing large motion, but small strains, leading to a geometrically exact formulation.

Acknowledgments: The authors gratefully acknowledge the support for this work from the National Natural Science Foundation of China (Grant No. 11272203)

A Definition of matrices

Several matrices used throughout the formulation are defined here. First, matrices $\underline{\underline{g}}$ and $\underline{\underline{B}}$ are defined as

$$\underline{\underline{g}} = \begin{bmatrix} 1 & 0 & 0 & 0 & 0 & \eta_3 & 0 & 0 \\ 0 & 1 & 0 & 0 & 0 & 0 & \eta_3 & 0 \\ 0 & 0 & 0 & 0 & 0 & 0 & 0 & 0 \\ 0 & 0 & 0 & 0 & 1 & 0 & 0 & 0 \\ 0 & 0 & 0 & 1 & 0 & 0 & 0 & 0 \\ 0 & 0 & 1 & 0 & 0 & 0 & 0 & \eta_3 \end{bmatrix}, \quad \underline{\underline{B}} = \begin{bmatrix} 0 & 0 & 0 \\ 0 & 0 & 0 \\ 0 & 0 & 1 \\ 0 & 1 & 0 \\ 1 & 0 & 0 \\ 0 & 0 & 0 \end{bmatrix} \frac{\partial}{\partial \eta_3}. \tag{51}$$

Next, matrices $\underline{\underline{\mathfrak{b}}}_1$ and $\underline{\underline{\mathfrak{b}}}_2$ are defined as

$$\underline{\underline{\mathfrak{b}}}_1 = \begin{bmatrix} 1 & 0 & 0 & 0 & 0 & 0 \\ 0 & 0 & 0 & 0 & 0 & 1 \\ 0 & 0 & 0 & 0 & 1 & 0 \end{bmatrix}, \tag{52a}$$

$$\underline{\underline{\mathfrak{b}}}_2 = \begin{bmatrix} 0 & 0 & 0 & 0 & 0 & 1 \\ 0 & 1 & 0 & 0 & 0 & 0 \\ 0 & 0 & 0 & 1 & 0 & 0 \end{bmatrix}. \tag{52b}$$

Another set of matrices, $\underline{\underline{\mathfrak{t}}}_1$ and $\underline{\underline{\mathfrak{t}}}_2$, are defined as

$$\underline{\underline{\mathfrak{t}}}_1 = \begin{bmatrix} 1 & 0 & 0 & 0 & 0 & 0 \\ 0 & 0 & 0 & 0 & 0 & 0 \\ 0 & 1 & 0 & 0 & 0 & 0 \\ 0 & 0 & 1 & 0 & 0 & 0 \\ 0 & 0 & 0 & 0 & 0 & 0 \\ 0 & 0 & 0 & 0 & 1 & 0 \\ 0 & 0 & 0 & 0 & 0 & 0 \\ 0 & 0 & 0 & -1 & 0 & 0 \end{bmatrix}, \quad \underline{\underline{\mathfrak{t}}}_2 = \begin{bmatrix} 0 & 0 & 0 & 0 & 0 & 0 \\ 0 & 1 & 0 & 0 & 0 & 0 \\ 1 & 0 & 0 & 0 & 0 & 0 \\ 0 & 0 & 0 & 0 & 0 & 0 \\ 0 & 0 & 1 & 0 & 0 & 0 \\ 0 & 0 & 0 & 0 & 0 & 0 \\ 0 & 0 & 0 & -1 & 0 & 0 \\ 0 & 0 & 0 & 0 & 1 & 0 \end{bmatrix}. \tag{53}$$

B Solution of the recursive system

The solution of recursive system (36) can be organized in a rational manner to minimize computational cost. First, matrices $\underline{h}^{(0)}$, $\underline{h}^{(1)}$, $\ldots \underline{h}^{(\mathcal{O})}$ are found using the following recurrence

$$\breve{\underline{\underline{E}}}\,\underline{h}^{(0)} = \underline{\mathcal{I}}, \tag{54a}$$

$$\breve{\underline{\underline{E}}}\,\underline{h}^{(1)} = \breve{\underline{\underline{H}}}_1 \left[\underline{h}^{(0)} \quad \underline{0}\right] + \breve{\underline{\underline{H}}}_2 \left[\underline{0} \quad \underline{h}^{(0)}\right], \tag{54b}$$

$$\begin{aligned} \breve{\underline{\underline{E}}}\,\underline{h}^{(k)} = {} & \breve{\underline{\underline{H}}}_1 \left[\underline{h}^{(k-1)} \quad \underline{0}\right] + \breve{\underline{\underline{H}}}_2 \left[\underline{0} \quad \underline{h}^{(k-1)}\right] \\ & + \breve{\underline{\underline{M}}}_{11} \left[\underline{h}^{(k-2)} \quad \underline{0} \quad \underline{0}\right] + \breve{\underline{\underline{M}}}_{12} \left[\underline{0} \quad \underline{h}^{(k-2)} \quad \underline{0}\right] + \breve{\underline{\underline{M}}}_{22} \left[\underline{0} \quad \underline{0} \quad \underline{h}^{(k-2)}\right]. \end{aligned} \tag{54c}$$

The following short-hand notation was introduced: matrix $\underline{h}^{(k)} = [\underline{h}^{(k)}_{k,0} \ldots \underline{h}^{(k)}_{0,k}]$ of size $N \times 8(k+1)$. All zero matrices appearing in eqs. (54) are of size $N \times 8$. The lowest order solution of recursive system (36) is then

$$\underline{\underline{X}}^{(0)}_{0,0} = \left[\ \underline{h}^{(0)} \ \middle|\ \underline{h}^{(1)} \ \middle|\ \underline{h}^{(2)} \ \middle|\ \ldots \ \middle|\ \underline{h}^{(\mathcal{O})} \ \right] \underline{\Lambda}, \tag{55}$$

where the vertical lines separate the orders of the expansion. At the first order, the solution is

$$\underline{\underline{X}}^{(1)}_{1,0} = \left[\ \underline{0} \ \middle|\ \underline{h}^{(0)} \ \ \underline{0} \ \middle|\ \underline{h}^{(1)} \ \ \underline{0} \ \middle|\ \ldots \ \middle|\ \underline{h}^{(\mathcal{O}-1)} \ \ \underline{0} \ \right] \underline{\Lambda}, \tag{56a}$$

$$\underline{\underline{X}}^{(1)}_{0,1} = \left[\ \underline{0} \ \middle|\ \underline{0} \ \ \underline{h}^{(0)} \ \middle|\ \underline{0} \ \ \underline{h}^{(1)} \ \middle|\ \ldots \ \middle|\ \underline{0} \ \ \underline{h}^{(\mathcal{O}-1)} \ \right] \underline{\Lambda}. \tag{56b}$$

At the second order, the solution is

$$\underline{\underline{X}}^{(2)}_{2,0} = \left[\ \underline{0}\ \middle|\ \underline{0}\ \ \underline{0}\ \middle|\ \underline{\underline{h}}^{(0)}\ \ \underline{0}\ \ \underline{0}\ \middle|\ \cdots\ \middle|\ \underline{\underline{h}}^{(\mathcal{O}-2)}\ \ \underline{0}\ \ \underline{0}\ \right]\underline{\underline{\Lambda}}, \tag{57a}$$

$$\underline{\underline{X}}^{(2)}_{1,1} = \left[\ \underline{0}\ \middle|\ \underline{0}\ \ \underline{0}\ \middle|\ \underline{0}\ \ \underline{\underline{h}}^{(0)}\ \ \underline{0}\ \middle|\ \cdots\ \middle|\ \underline{0}\ \ \underline{\underline{h}}^{(\mathcal{O}-2)}\ \ \underline{0}\ \right]\underline{\underline{\Lambda}}, \tag{57b}$$

$$\underline{\underline{X}}^{(2)}_{0,2} = \left[\ \underline{0}\ \middle|\ \underline{0}\ \ \underline{0}\ \middle|\ \underline{0}\ \ \underline{0}\ \ \underline{\underline{h}}^{(0)}\ \middle|\ \cdots\ \middle|\ \underline{0}\ \ \underline{0}\ \ \underline{\underline{h}}^{(\mathcal{O}-2)}\ \right]\underline{\underline{\Lambda}}. \tag{57c}$$

Higher-order solutions follow a similar pattern.

References

[1] S.P. Timoshenko and S. Woinowsky-Krieger. *Theory of Plates and Shells*. McGraw-Hill Book Company, New York, 1959.

[2] O.A. Bauchau and J.I. Craig. *Structural Analysis with Application to Aerospace Structures*. Springer, Dordrecht, Heidelberg, London, New-York, 2009.

[3] E. Reissner. The effect of transverse shear deformation on the bending of elastic plates. *Zeitschrift für angewandte Mathematik und Physik*, 12:A.69–A.77, 1945.

[4] E. Reissner. On bending of elastic plates. *Quarterly of Applied Mathematics*, 5:55–68, 1947.

[5] R.D. Mindlin. Influence of rotatory inertia and shear on flexural motions of isotropic elastic plates. *Journal of Applied Mechanics*, 18:31–38, 1951.

[6] L. Librescu. *Elastostatics and Kinetics of Anisotropic and Heterogeneous Shell-Type Structures*. Noordhoff International Publishing, Leyden, 1975.

[7] J.M. Whitney. *Structural Analysis of Laminated Anisotropic Plates*. Technomic Publishing Company, Lancaster, 1987.

[8] J.N. Reddy. *Mechanics of Laminated Composite Plates*. CRC Press, Boca Raton, 1996.

[9] R.M. Christensen. *Mechanics of Composite Materials*. John Wiley & Sons, New York, 1979.

[10] S.W. Tsai and H.T. Hahn. *Introduction to Composite Materials*. Technomic Publishing Co., Inc., Westport, CT, 1980.

[11] K.H. Lo, R.M. Christensen, and F.M. Wu. A higher-order theory of plate deformation, II: Laminated plates. *Journal of Applied Mechanics*, 44:669–676, 1977.

[12] J.N. Reddy. A simple higher-order theory for laminated composite plates. *Journal of Applied Mechanics*, 51(4):745–752, 1984.

[13] B.N. Pandya and T. Kant. Higher-order shear deformable theories for flexure of sandwich plates-finite element evaluations. *International Journal of Solids and Structures*, 24(12):1267–1286, 1988.

[14] H. Murakami. Laminated composite plate theory with improved in-plane responses. *Journal of Applied Mechanics*, 53:661–666, 1986.

[15] M. Cho and R. Parmerter. Efficient higher-order composite plate theory for general lamination configurations. *AIAA Journal*, 31(7):1299–1306, 1993.

[16] M.D. Sciuva. Multilayered anisotropic plate models with continuous interlaminar stresses. *Composite Structures*, 22(3):149–167, 1992.

[17] E. Carrera. Mixed layer-wise models for multilayered plates analysis. *Composite Structures*, 43(1):57–70, 1998.

[18] Y.B. Cho and R.C. Averill. First-order zig-zag sublaminate plate theory and finite element model for laminated composite and sandwich panels. *Composite Structures*, 50:1–15, 2000.

[19] E. Carrera. Developments, ideas, and evaluations based upon Reissner's mixed variational theorem in the modeling of multilayered plates and shells. *Applied Mechanics Reviews*, 54:301–329, 2001.

[20] E. Carrera and L. Demasi. Classical and advanced multilayered plate elements based upon PVD and RMVT. Part 1: Derivation of finite element matrices. *International Journal for Numerical Methods in Engineering*, 55:191–231, 2002.

[21] K.O. Friedrichs and R.F. Dressler. A boundary-layer theory for elastic plates. *Communications on Pure and Applied Mathematics*, 14(1):1–33, 1961.

[22] A. Kalamkarov. *Composite and Reinforced Elements of Construction*. John Wiley & Sons, Chichester, New York, 1992.

[23] V.L. Berdichevsky. Variational-asymptotic method of shell theory construction. *Prikladnaya Matematika y Mekanika*, 43(4):664–687, 1979.

[24] V.L. Berdichevsky. On the energy of an elastic rod. *Prikladnaya Matematika y Mekanika*, 45(4):518–529, 1982.

[25] V.G. Sutyrin and D.H. Hodges. On asymptotically correct linear laminated plate theory. *International Journal of Solids and Structures*, 33:3649–3671, 1996.

[26] V.G. Sutyrin. Derivation of plate theory accounting asymptotically correct shear deformation. *Journal of Applied Mechanics*, 64:905–915, 1997.

[27] W.B. Yu, D.H. Hodges, and V.V. Volovoi. Asymptotic generalization of Reissner-Mindlin theory: Accurate three-dimensional recovery for composite shells. *Computer Methods in Applied Mechanics and Engineering*, 191(44):5087–5109, 2002.

[28] W.B. Yu and D.H. Hodges. A geometrically nonlinear shear deformation theory for composite shells. *Journal of Applied Mechanics*, 71(1):1–9, 2004.

[29] J. S. Kim. An asymptotic analysis of anisotropic heterogeneous plates with consideration of end effects. *Journal of Mechanics of Materials and Structures*, 4(9):1535–1553, 2010.

[30] P. Masarati and G.L. Ghiringhelli. Characterization of anisotropic, non-homogeneous plates with piezoelectric inclusions. *Computer & Structures*, 83:1171–1190, 2005.

[31] F. Gruttmann and W. Wagner. A coupled two-scale shell model with applications to layered structures. *International Journal for Numerical Methods in Engineering*, 94(13):1233–1254, 2013.

[32] O.A. Bauchau. *Flexible Multibody Dynamics*. Springer, Dordrecht, Heidelberg, London, New-York, 2011.

[33] N.J. Pagano. Exact solutions for composite laminates in cylindrical bending. *Journal of Composite Materials*, 3:398–411, 1969.

[34] J.R. Fan and J.Q. Ye. An exact solution for the statics and dynamics of laminated thick plates with orthotropic layers. *International Journal of Solids and Structures*, 26(5):655–662, 1990.

[35] H.-R. Meyer-Piening. Experiences with "exact" linear sandwich beam and plate analyses regarding bending, instability and frequency investigations. In *Proceedings of the Fifth International Conference on Sandwich Constructions*, volume 1, pages 37–48, 2000.

[36] E. Carrera and L. Demasi. Two benchmarks to assess two-dimensional theories of sandwich, composite plates. *AIAA Journal*, 41:1356–1362, 2003.